

46 **1 Introduction**

47

48 During the Last glacial maximum (LGM), the Patagonian Ice Sheet (PIS) covered the Andes
49 mountains from 38°S to 55°S, with an estimated sea-level equivalent ice volume of 1.5 meters
50 (Davies et al., 2020). At the northernmost extent of the PIS, across an area presently known as the
51 Chilean Lake District (CLD: 37°S-41.5°S), the LGM to deglacial ice behavior and related climate
52 forcings has been a subject of historical interest (Mercer, 1972; Porter, 1981; Lowell et al., 1995;
53 Andersen et al., 1999; Denton et al., 1999; Glasser et al., 2008, Moreno et al., 2015; Kilian and
54 Lamy, 2012; Lamy et al., 2010), and have served as important constraints towards understanding
55 the drivers of ice sheet change across centennial to millennial timescales. Currently, PATICE
56 (Davies et al., 2020) serves as the latest and most complete reconstruction of the entire PIS during
57 the LGM and last deglaciation. Across the CLD (Figure 1), the LGM ice limits are only well
58 constrained by terminal moraines in the southwest and western margins (Denton et al., 1999;
59 Glasser et al., 2008, Moreno et al., 2015). However, due to a lack of geomorphological and
60 geochronologic constraints on ice margin change following the LGM, the reconstructed
61 deglaciation remains highly uncertain.

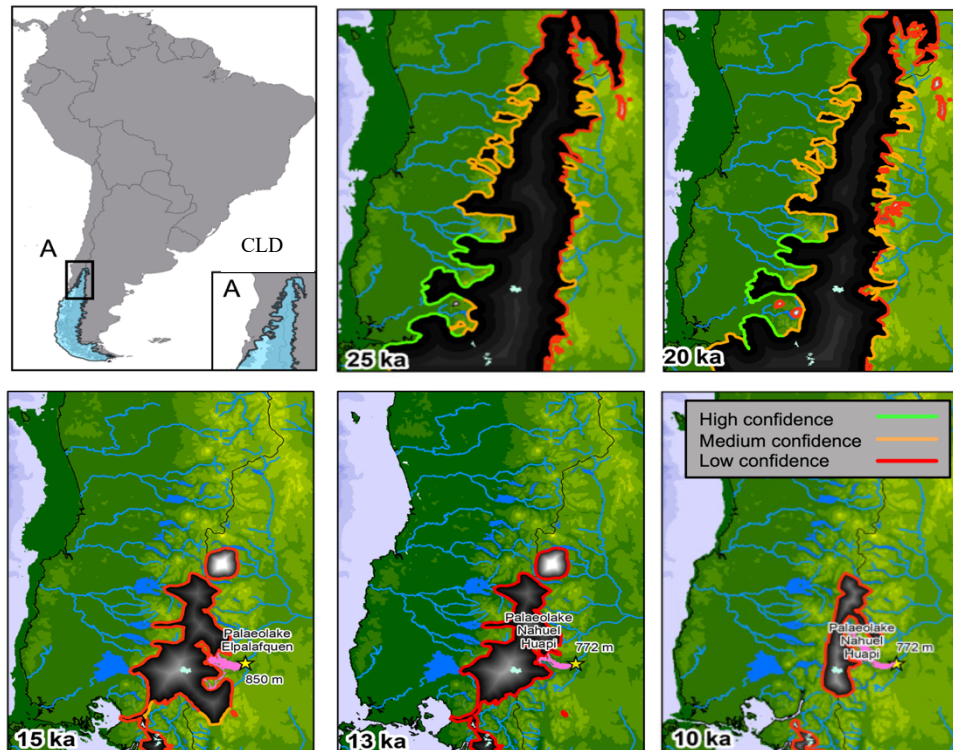


Figure 1. Location of the study area across the Chilean Lake District (CLD; Upper Left Panel). The reconstructed ice extent from PATICE for the PIS across the CLD at 25 ka, 20 ka, 15 ka, 13 ka, and 10 ka are taken from Davies et al., 2020. The color of the line marking the reconstructed ice extent corresponds to the confidence in the reconstruction as described in section 3.3.

62 While deglacial warming is a primary driver of ice retreat across the CLD, evidence suggests that
63 variations in precipitation patterns influenced the timing and magnitude of this retreat (Moreno et
64 al., 1999; Rojas et al., 2009). The wintertime climate across South America is strongly influenced
65 by the southern annular mode (SAM; Hartmann and Lo, 1998), for which its phase and strength is
66 regulated by changes in the difference of zonal mean sea-level pressure between mid (40°S) and

67 high latitudes (65°S). The SAM in turn modulates the strength and position of the southern
68 westerly winds (SWW) over decadal to multi-centennial timescales, which exert a large control on
69 the synoptic scale hydrologic and heat budget (Garreaud et al., 2013). During the LGM and last
70 deglaciation, paleoclimate data indicates that the position, strength, and extent of the SWW varied
71 latitudinally, migrating southward during warmer intervals and northward during cooler intervals,
72 ultimately altering overall ice sheet mass balance (Mercer, 1972; Denton et al., 1999; Lamy et al.,
73 2010; Kilian and Lamy, 2012; Boex et al., 2013). Terrestrial paleoclimate proxies that indicate
74 that the CLD was wetter during the LGM and early deglaciation have been used to support the
75 idea that the SWW migrated northward of 41°S across the CLD (Moreno et al., 1999; Moreno et
76 al., 2015; Moreno and Videla, 2018; Diaz et al., 2023). Additionally, these proxies indicate a
77 switch from hyper humid to humid conditions around 17,300 cal yr BP, which was inferred by
78 Moreno et al. (2015) to indicate the poleward migration of the SWW south of the CLD.

79
80 However, inferring changes in the SWW across the last deglaciation from paleoclimate proxies
81 can be problematic as outlined by Kohfeld et al. (2013) who compiled an extensive dataset of
82 paleoclimate archives that record changes in moisture, precipitation-evaporation balance, ice
83 accumulation, runoff and precipitation, dust deposition, and marine indicators of sea surface
84 temperature, ocean fronts, and biologic productivity. Kohfeld et al. (2013) conclude that
85 environmental changes inferred from existing paleoclimate data could be potentially explained by
86 a range of plausible scenarios for the state and change of the SWW during the LGM and last
87 deglaciation, such as a strengthening, poleward or equatorward migration, or no change. Climate
88 model results from Sime et al. (2013) indicate that the reconstructed changes in moisture from
89 Kohfeld et al. (2013) can be simulated well without invoking large shifts or changes in strength to
90 the SWW. This discrepancy also exists amongst climate models which diverge on whether the
91 LGM SWW was shifted equatorward or poleward, and was stronger or weaker than present day
92 (Togweiler et al., 2006; Menviel et al., 2008; Rojas et al., 2009; Rojas et al., 2013; Sime et al.,
93 2013; Jiang et al., 2020). Therefore, from paleoclimate proxies and climate models, we still do
94 not have a firm understanding of how the SWW may have changed during the last deglaciation,
95 and how these variations may have influenced the deglaciation of the PIS.

96
97 Early paleo ice sheet modelling experiments across the PIS have focused on evaluating the
98 relationship between the simulated LGM ice sheet geometry in response to spatially uniform
99 temperature change (Hulton et al., 2002; Sugden et al., 2002; Hubbard et al., 2005). While these
100 early simulations provided constraints on PIS areal extent, ice volume, and sensitivity to LGM
101 temperature depressions, spatially varying temperature and precipitation were not considered.
102 Recently, Yan et al. (2022) simulated the PIS behavior at the LGM using an ensemble of climate
103 model output from the Paleoclimate Modelling Intercomparison Project (PMIP4; Kageyama et al.,
104 2021). Results best matching the empirical reconstructions from PATICE (Davies et al., 2020)
105 suggest that reduction in temperature was likely the main driver of PIS LGM extent, although the
106 authors found that variation in regional LGM precipitation anomaly can have large impacts on the
107 simulated ice sheet geometry. This evidence is supported by recent glacier modelling across the
108 northeastern Patagonian Andes which suggests that increases in precipitation during the
109 termination of the LGM are necessary to achieve modeled fit with reconstructed glacier extent
110 (Muir et al., 2023; Leger et al., 2021b). Additionally, Martin et al. (2022) found that precipitation
111 greater than present day is needed to explain late glacial and Holocene ice readvance of the Monte
112 San Lorenzo ice cap, lying to the southeast of the current Northern Patagonian Ice Field. These

113 regional studies therefore provide further evidence that late glacial and deglacial variability in
114 precipitation, perhaps driven by changes in the SWW, influenced PIS retreat and readvance over
115 numerous timescales.

116
117 To advance our understanding of the last glacial and deglacial ice behavior across the CLD, we
118 use a numerical ice sheet model to simulate the LGM ice geometry and deglacial ice retreat using
119 transiently evolving boundary conditions from a climate model simulation of the last 21,000 years
120 (TraCE-21ka; Liu et al., 2009; He et al., 2013) which simulates large scale variability in the
121 strength and position of the SWW (Jiang and Yan, 2020). Because there is a lack of transiently
122 evolving ice sheet model simulations of the PIS across the last deglaciation, our aim is to provide
123 possible constraints on the nature of ice retreat across the CLD region, from which the
124 reconstructions (PATICE; Davies et al., 2020) are uncertain. Also, by assessing the sensitivity of
125 our ice sheet experiments to a range of climatic boundary conditions, we aim to provide additional
126 insight into the dominant climatic controls on the deglacial evolution of the PIS in the CLD region.

127

128 **2 Methods: Model description and setup**

129

130 **2.1 Ice sheet model**

131

132 In order to simulate the ice margin migration across the CLD during the LGM and last deglaciation,
133 we use the Ice Sheet and Sea-level System Model (ISSM), a thermomechanical finite-element ice
134 sheet model (Larour et al., 2012). Because of the high topographic relief across the CLD and
135 associated impact on ice flow, we use a higher-order approximation to solve the momentum
136 balance equations (Dias dos Santos et al., 2022). This ice flow approximation is a depth-integrated
137 formulation of the higher-order approximation of Blatter (1995) and Pattyn (2003), which allows
138 for an improved representation of ice flow compared with more traditional approaches in paleo-
139 ice flow modelling (e.g., Shallow Ice Approximation or hybrid approaches; Hubbard et al., 2005;
140 Leger et al., 2021b; Yan et al., 2022), while allowing for reasonable computational efficiency. Our
141 model domain comprises the northernmost LGM extent of the PIS across the CLD, extending
142 beyond the LGM ice extent reconstructed from Davies et al. (2020) and ends along the northern
143 shore of the Golfo de Ancud (Figure 2).

144

145 We rely on anisotropic mesh adaptation to create a non-uniform model mesh that varies based
146 upon gradients in bedrock topography from the General Bathymetric Chart of the Oceans
147 (GEBCO; GEBCO Bathymetric Compilation Group, 2021), a terrain model for ocean and land.
148 For the land component, the GEBCO model uses version 2.2 of the Surface Radar Topography
149 Mission data (SRTM15_plus; Tozer et al., 2019), to create a 15 arc second gridded output of terrain
150 elevation relative to sea level. Our ice sheet model horizontal mesh resolution varies from 3 km
151 in areas of low bedrock relief to 450 meters in areas where gradients in the bedrock topography is
152 high and comprises 40,000 model elements. We impose no boundary conditions of ice flow and
153 thickness at the southern extent of our model domain. Due to the north-south nature of the
154 simulated ice divide during the last deglaciation (see Figure 4), inflow from the south and into our
155 model domain is minimal and was found to not impact our results.

156

157

158

159
160
161
162
163
164
165
166
167
168
169
170
171
172
173
174
175
176
177
178
179
180
181
182
183
184
185
186
187
188
189

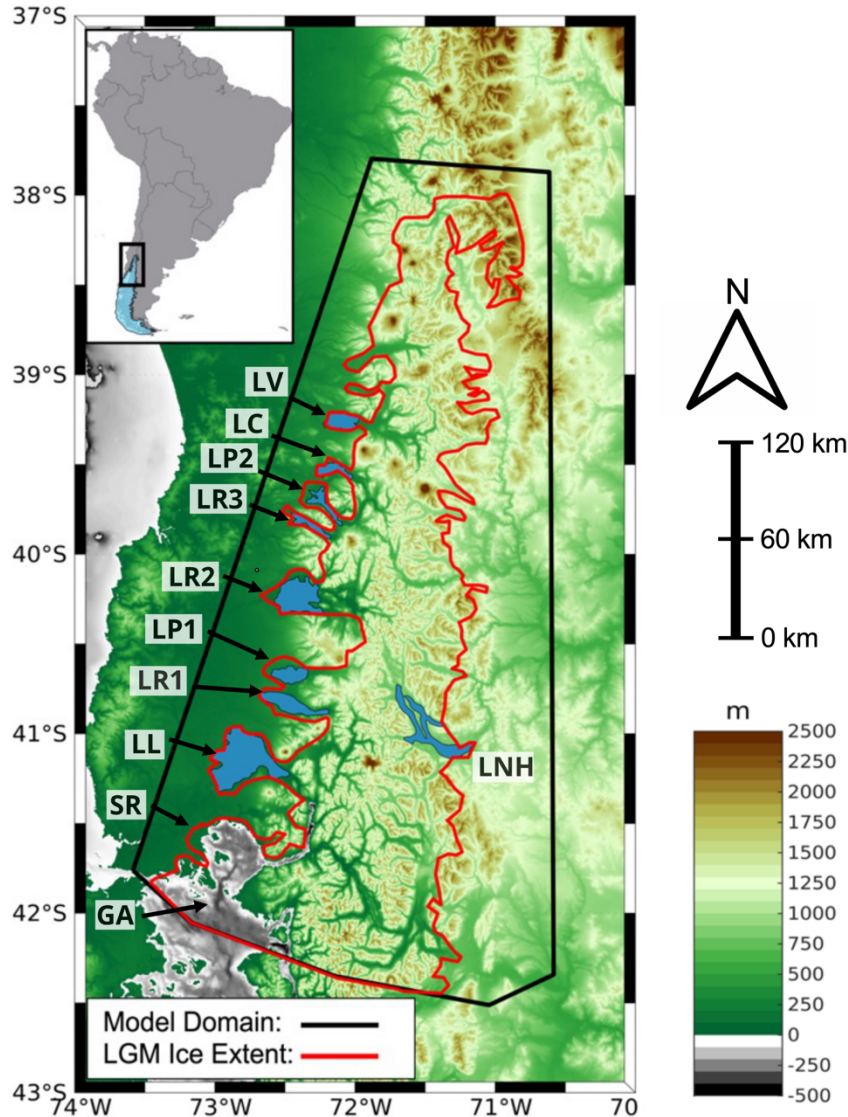


Figure 2. Bedrock topography for our study area (meters). Our model domain (shown as the black line), encompasses the reconstructed LGM ice limit (shown in red) from PATICE (Davies et al., 2020). Present day lakes are shown in blue, with abbreviated names as: SR (Seno de Reloncaví), GA (Golfo de Ancud), LL (Lago Llanquihue), LR1 (Lago Rupanco), LP1 (Lago Puyehue), LR2 (Lago Ranco), LR3 (Lago Riñihue), LP2 (Lago Panguipulli), LC (Lago Calafquén), LV (Lago Villarica), LNH (Lago Nahuel Huapi).

190 Although geomorphological evidence suggests that while southernmost glaciers across the PIS
191 may have been temperate with warm based conditions during the LGM, there may have been
192 periods where ice lobes were polythermal (Darvill et al., 2016). However, recent ice flow
193 modelling (Leger et al., 2021b) suggests that varying ice viscosity mainly impacts the
194 accumulation zone thickness in simulations of paleoglaciers in Northeastern Patagonia, with
195 minimal impacts on overall glacier length and extent. Accordingly, based on sensitivity tests (see
196 supplement section S1), our model is 2-dimensional and we do not solve for ice temperature and
197 viscosity allowing for increased computational efficiency. For our purposes, we use Glen’s flow

198 law (Glen, 1955) and set the ice viscosity following the rate factors in Cuffey and Paterson (2010)
199 assuming an ice temperature of -0.2°C . We use a linear friction law (Budd et al., 1979)

$$200 \tau_b = -k^2 N u_b \quad (1)$$

202 where τ_b represents the basal stress, N represents the effective pressure, and u_b is the magnitude
203 of the basal velocity. Here $N = g(\rho_i H + \rho_w Z_b)$, where g is gravity, H is ice thickness, ρ_i is the
204 density of ice, ρ_w is the density of water, and Z_b is bedrock elevation following Cuffey and Paterson
205 (2010).

207 The spatially varying friction coefficient, k , is constructed following Åkesson et al. (2018):

$$208 k = 200 \times \frac{\min[\max(0, z_b + 600), z_b]}{\max(z_b)} \quad (2)$$

210 where z_b is the height of the bedrock with respect to sea level. Using this parameterization, basal
211 friction is larger across high topographic relief and lower across valleys, and areas below sea level.

212 To account for the influence of glacial isostatic adjustment (GIA), we prescribe a transiently
213 evolving reconstruction of relative sea level from the global GIA model of the last glacial cycle
214 from Caron et al. (2018). This includes three physical components: 1) Bedrock vertical motion
215 2.) Eustatic sea level, and 3.) Geoid changes. The time series we use to prescribe GIA is from the
216 model average of an ensemble of GIA forward model estimations from Caron et al., 2018. The
217 prescribed GIA is in good agreement (Figure S2) with a reconstruction of relative sea-level change
218 from an isolation basin in central Patagonia (Troch et al., 2022). This methodology has been
219 applied in recent modelling following Cuzzone et al. (2019) and Briner et al. (2020).

222 2.2 Experimental Design

223 In order to simulate the ice history at the LGM and across the last deglaciation we use climate
224 model output from the National Center for Atmospheric Research Community Climate System
225 Model (CCSM3) TraCE-21ka transient climate simulation of the last deglaciation (Liu et al., 2009;
226 He et al., 2013). Monthly mean output of temperature and precipitation are used from these
227 simulations as inputs to our glaciological model (full climate forcings details are further described
228 in section 2.4) and we use the monthly mean output every 50 years across the last deglaciation.
229 Large, multi-proxy reconstructions from He and Clark (2022), Liu et al. (2009), He et al. (2011),
230 and Shakun et al. (2012; 2015) have all demonstrated good agreement between TRACE 21k and
231 a wide variety of paleo-proxy data during the last deglaciation that include records from the West
232 Antarctic and South America.

234 2.3 Surface Mass Balance

235 In order to simulate the deglaciation of the PIS across our model domain we require inputs of
236 temperature and precipitation to estimate the surface mass balance. To derive snow and ice melt
237 we use a positive degree day model (Tarasov and Peltier, 1999; Le Morzadec et al., 2015; Cuzzone
238 et al., 2019; Briner et al., 2020). Our degree day factor for snow melt is $3 \text{ mm } ^{\circ}\text{C}^{-1}\text{day}^{-1}$ and $6 \text{ mm } ^{\circ}\text{C}^{-1}\text{day}^{-1}$
239 for bare ice melt, and we use a lapse rate of $6 \text{ } ^{\circ}\text{C}/\text{km}$ to adjust the temperature of the
240

241 climate forcings to surface elevation, which are within a range of typical values used to model
 242 contemporary and paleo glaciers across Patagonia (see Fernandez et al., 2016 Table 3; Yan et al.,
 243 2022). The hourly temperatures are assumed to have a normal distribution, of standard
 244 deviation 3.5 degrees Celsius around the monthly mean. An elevation-dependent desertification
 245 is included (Budd and Smith, 1981) which reduces precipitation by a factor of 2 for every kilometer
 246 change in ice sheet surface elevation. We note that the values in the surface mass balance
 247 parameters were chosen to provide a reasonable fit within 5% between the simulated LGM ice sheet
 248 area and the reconstructed ice area from PATICE (see Figure 4 and 10).

249

250 2.4 Climate forcings

251

252 In order to scale monthly temperature and precipitation across the LGM and last deglaciation we
 253 applied a commonly used modeling approach (Pollard et al., 2012; Seguinot et al., 2016; Golledge
 254 et al., 2017; Tigchlaar et al., 2019; Clark et al., 2020; Briner et al., 2020; Cuzzone et al., 2022; Yan

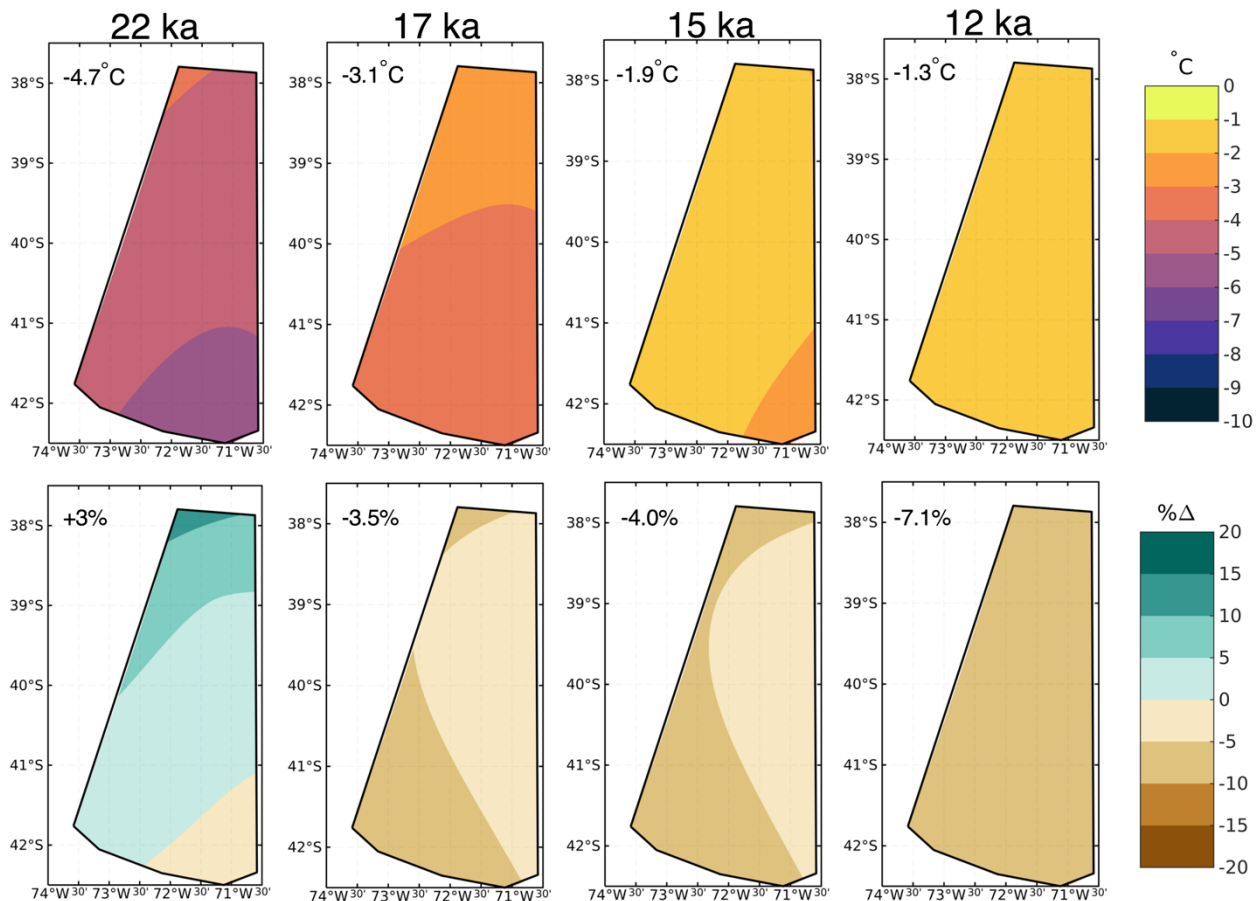


Figure 3. The bilinearly summer (DJF) temperature (top row) and winter (JJA) precipitation anomalies (bottom row) from TraCE-21ka at 22 ka, 17 ka, 16 ka, and 12 ka. Anomalies are taken as the difference between the corresponding time period and preindustrial (LGM-PI), with the precipitation anomalies expressed as the percent difference from preindustrial. The area averaged value of the anomaly is shown in the upper left corner of each

255

256 et al., 2022; equations 3 and 4). First, we use the monthly mean climatology of temperature and
 257 precipitation for the period 1979-2018 ($\bar{T}_{(1979-2018)}$, $\bar{P}_{(1979-2018)}$) from the Center for Climate

258 Resilience Research Meteorological dataset version 2.0 (CR2MET; Boisier et al., 2018). This
 259 output, which uses information from a climate reanalysis and is calibrated against rain-gauge
 260 observations, is provided at 5 km spatial resolution.

261
 262 We then bilinearly interpolate these fields onto our model mesh.

$$264 T_t = \bar{T}_{(1979-2018)} + \Delta T_t \quad (3)$$

$$266 P_t = \bar{P}_{(1979-2018)} + \Delta P_t \quad (4)$$

267
 268 Next, anomalies of the monthly temperature and precipitation fields from TraCE-21ka (Liu et al.,
 269 2009; He et al., 2013) are computed as the difference from the preindustrial control run and
 270 interpolated onto our model mesh (ΔT_t and ΔP_t). These anomalies are added to the contemporary
 271 monthly mean as shown in equations 3 and 4, to produce the monthly temperature and precipitation
 272 fields at LGM and across the last deglaciation (T_t and P_t). In Figure 3 anomalies from preindustrial
 273 of summer temperature and winter precipitation are shown for 22 ka, 17 ka, 15 ka, and 12 ka.

275 2.5 Ice front migration and iceberg calving

276
 277 We simulate calving where the PIS interacts with ocean, but do not include any treatment of
 278 calving in proglacial lakes (see section 4.3). We track the motion of the ice front using the level-
 279 set method described in Bondzio et al. (2016; equation 3) in which the ice velocity v_f , is a function
 280 of the ice velocity vector at the ice front (v), the calving rate (c), the melting rate at the calving
 281 front (\dot{M}), and where n is the unit normal vector pointing horizontally outward from the calving
 282 front. For these simulations the melting rate is assumed to be negligible compared to the calving
 283 rate, so \dot{M} is set to 0.

$$285 v_f = v - (c + \dot{M}) n \quad (5)$$

286
 287 To simulate calving we employ the more physically based Von Mises stress calving approach
 288 (Morlighem et al., 2016) which relates the calving rate (c) to the tensile stresses simulated within
 289 the ice, where $\tilde{\sigma}$ is the von Mises tensile strength, $\|v\|$ is the magnitude of the horizontal ice
 290 velocity, and σ_{max} is the maximum stress threshold which has separate values for tidewater and
 291 floating ice, namely 1 MPa and 200 kPa.

$$293 c = \|v\| \frac{\tilde{\sigma}}{\sigma_{max}} \quad (6)$$

294
 295 The ice front will retreat if von Mises tensile strength exceeds the user defined stress threshold.
 296 This calving law has been applied in Greenland to assess marine terminating icefront stability
 297 (Bondzio et al., 2016; Morlighem et al., 2016; Choi et al., 2021; Cuzzone et al., 2022) and for our
 298 simulations applies where ocean is present such as the Seno de Reloncaví and the Golfo de Ancud
 299 (see Figure 2).

301 3 Results

302

303 **3.1 Simulated LGM state**

304

305 In order to arrive at a steady state LGM ice geometry, we first initialize our model with an ice-free
306 configuration. A constant LGM monthly climatology of temperature and precipitation are then
307 applied, as well as the prescribed GIA from Caron et al. (2018). We allow the ice sheet to relax for
308 10,000 years, during which, the ice sheet is free to grow and expand until it reaches a steady state
309 ice geometry and volume, in equilibrium with the climate forcings.

310

311 At 22 ka, Trace-21ka simulates an area averaged summertime (DJF) cooling of 4.7°C relative to
312 the PI across our model domain (Figure 3). The LGM cooling increases from north to south, with
313 the greatest magnitude of cooling occurring across the southern portion of our model domain of
314 up to 6°C. During winter (JJA), Trace-21ka simulates an overall wetter climate across our model
315 domain during the LGM relative to the PI. While the area-averaged LGM precipitation anomaly
316 is small (3% higher), the LGM precipitation anomaly increases from south to north, with Trace-
317 21ka simulating 10-15% more wintertime precipitation during the LGM than the PI across the
318 northern portion of the model domain.

319

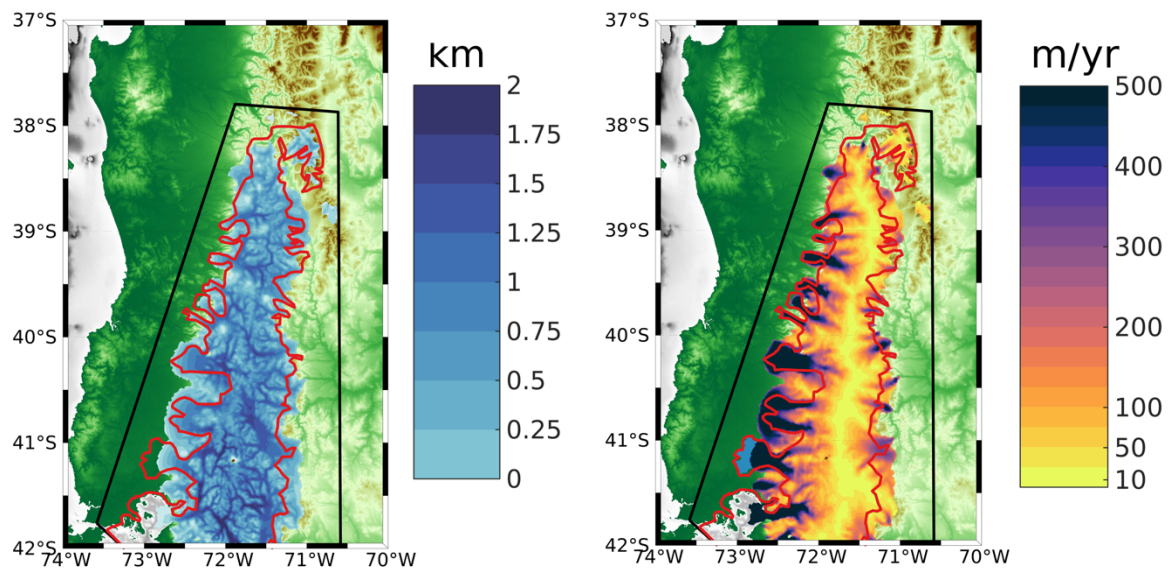


Figure 4. The simulated LGM ice thickness (km; left panel) and the simulated LGM ice surface velocity (m/yr; right panel) is shown. The black outline denotes our ice sheet model boundary, and the red line denotes the LGM reconstructed ice extent from PATICE (Davies et al., 2020).

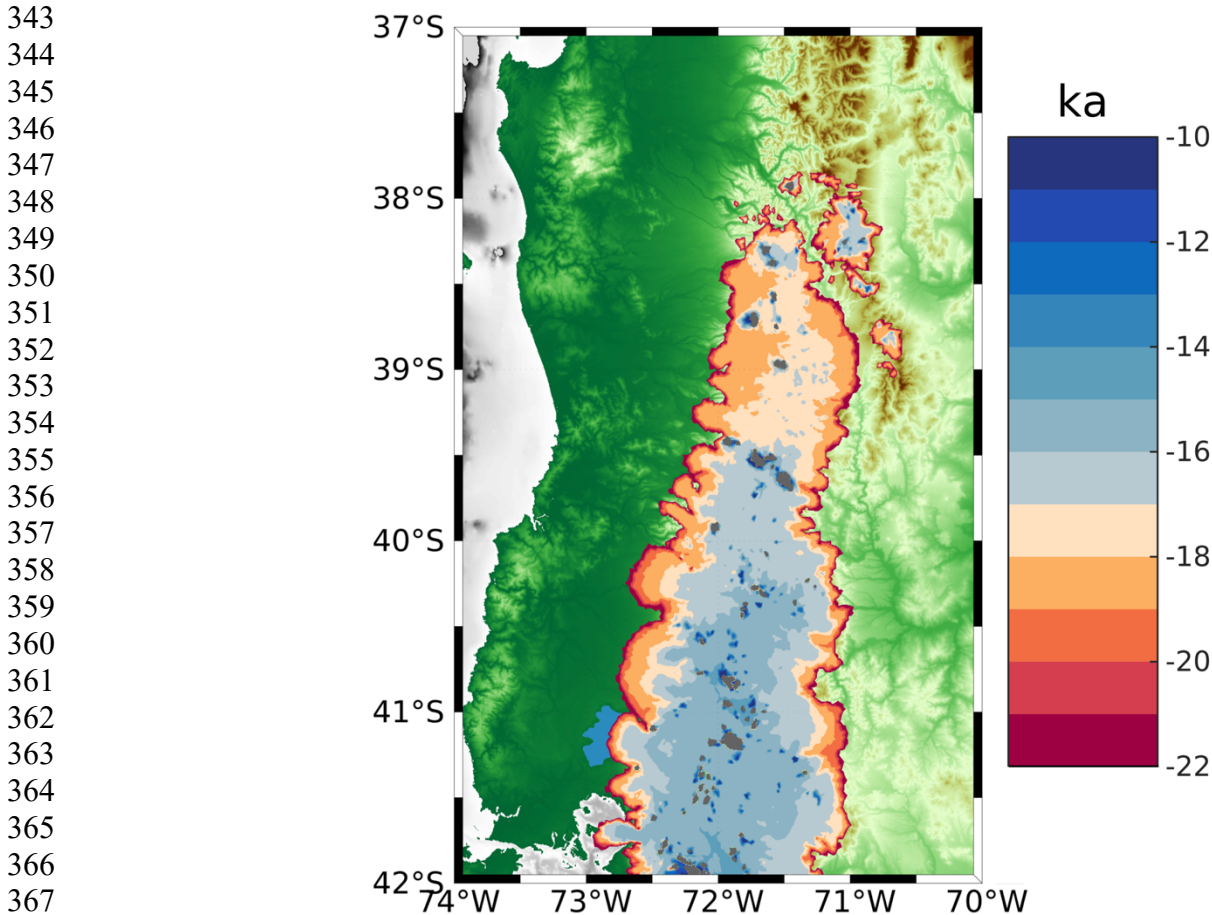
320 Bedrock elevation increases from west to east, with deep valleys interspersed across most of our
321 model domain (Figure 2). LGM ice thickness is greatest in these valleys (upwards of 2000 meters)
322 where driving stresses dominate and where bedrock geometry controls the flow of ice from higher
323 terrain and through these valleys (Figure 4). Across the highest terrain such as the many volcanoes
324 across the CLD, ice is comparatively thinner than the surrounding valleys. An ice divide is present
325 as slow ice velocities in the interior of the ice sheet, which give way to fast flowing outlet glaciers
326 especially on the western margin of the CLD where velocities reach in excess of 500 m/yr and in
327 some location up to 2 km/yr. The simulated LGM ice sheet area across the CLD is 414,120 km²,

328 which is within 1% of the area calculated from the PATICE reconstruction (414,690 km²; Figure
329 10). This agreement is in part due to the tuning of our degree day factors as discussed in section
330 2.3, and gives confidence to our ability to simulate a reasonable LGM ice sheet across the CLD
331 and throughout the last deglaciation.
332

333 3.2 Simulation of the Last Deglaciation

334
335 Monthly mean temperature and precipitation, taken every 50 years from the TraCE-21ka (Liu et
336 al., 2009; He et al., 2013) experiment is used to drive our simulation of ice history across the last
337 deglaciation (22 ka – 10 ka). The transient simulation is initialized with the LGM ice sheet
338 geometry shown in Figure 4, and is run forward with the appropriate climate boundary conditions
339 until 10 ka.
340

341 3.2.1 Pattern of Deglaciation



368
369 Figure 5. The simulated deglaciation age for the transient simulation from the LGM to 10 ka. The gray color
370 indicates where ice persists after 10 ka.

371 From the resulting transient simulation, we calculate the timing of deglaciation across our model
372 domain (Figure 5) as the youngest age at which grid points become ice free. Our map of the

373 simulated deglaciation can be paired with a timeseries of the rate of ice mass change (Figure 6) to
374 highlight some key features in the magnitude and timing of ice retreat between 22 ka and 10 ka.

375
376 Between 22 ka to 19 ka, the ice sheet undergoes periods of minor to moderate ice mass loss and
377 gain in an interval of time where summer temperature anomalies (Figure 6) and the corresponding
378 ice margin remain relatively stable (Figure 5). Between 19 ka and 18.5 ka, coincident with a rise
379 in summertime temperature (Figure 6), a pulse of ice mass loss exceeding 5,000 GT/century occurs
380 before trending toward minimal ice mass loss around 18 ka as the rise in summer temperature
381 levels off. During this time interval, the ice margin pulls back considerably towards higher terrain
382 across the northern portion of the model domain (Figure 5), and many of the fast-flowing outlet
383 glaciers on the western margin retreat back towards the ice sheet interior. Between 18 ka to 16.2
384 ka, summer temperature rises steadily $\sim 1.2^\circ\text{C}$ and is punctuated with an abrupt warming of $\sim 0.5^\circ\text{C}$
385 at 16 ka (Figure 6). During this interval, ice mass loss remains high and steady at ~ 1000
386 GT/century with pulses of increased mass loss at 17.8 ka, 16.8 ka, and 16 ka varying between
387 2000-5000 GT/century (Figure 6).

388

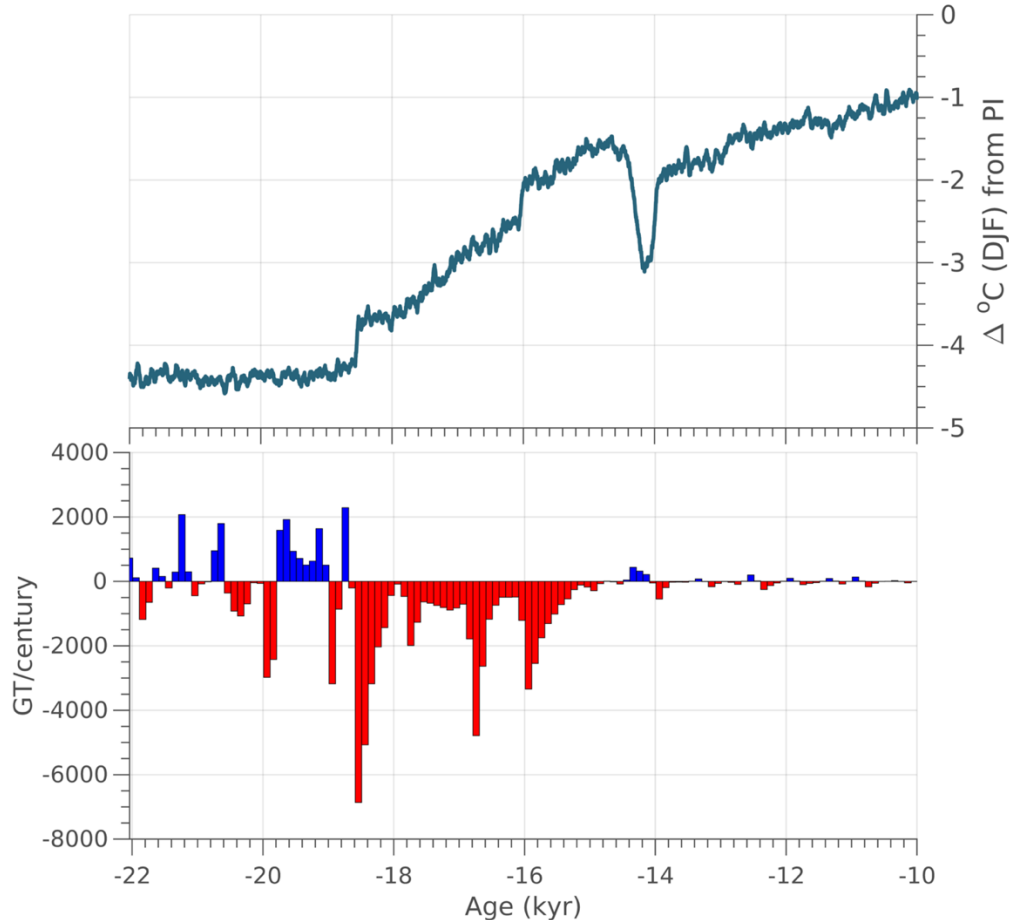


Figure 6. Top Panel: The TraCE-21ka Summer (DJF) temperature anomaly taken as the difference from the preindustrial period, area averaged across our model domain. Bottom Panel: The simulated ice mass change calculated in GT/century across the last deglaciation (22 ka to 10 ka). Red indicates ice mass loss, and blue indicates ice mass gain.

389

390 By 17 ka, the northern portion of the model domain (north of 39.5°S), has generally become ice
391 free for the exception of the highest terrain (e.g., mountain glaciers). By 16 ka, between 39.5°S
392 and 40.5°S, ice remains only on the highest terrain (Figure 5), however ice cover persists south of
393 40.5°S. Between 16 ka and 15 ka, summer temperature rises $\sim 0.5^\circ\text{C}$ (Figure 6) and the remaining
394 ice sheet retreats south of 40.5°S. By 15 ka, there is no evidence of an ice sheet, with only
395 mountain glaciers and small ice caps (e.g., Cerro Tronador) existing across the high terrain
396 throughout the model domain (Figure 5).

397
398 After 15 ka, TraCE-21ka simulates a short and abrupt Antarctic Cold Reversal (ACR) between
399 14.6 ka and 14 ka (Figure 6), before temperatures continue to rise into the early Holocene. There
400 is only a minor ice mass gain (e.g., <500 GT/yr) during the ACR, and minimal fluctuation in ice
401 mass after 14 ka. By 10 ka, only small mountain glaciers persist across the high terrain and
402 volcanoes of the CLD (gray color in Figure 5).

403 404 3.2.2 Sensitivity Tests

405
406 To better assess how changes in precipitation may modulate the deglaciation across the CLD we
407 perform additional sensitivity tests. We refer to the simulation discussed above as our *main*
408 *simulation*, where the climate boundary conditions of temperature and precipitation varied
409 temporally and spatially across the last deglaciation. Three more simulations are performed where
410 temperature is allowed to vary across the last deglaciation, but precipitation remains fixed at a
411 given magnitude for a particular time interval. Each experiment is listed below as:

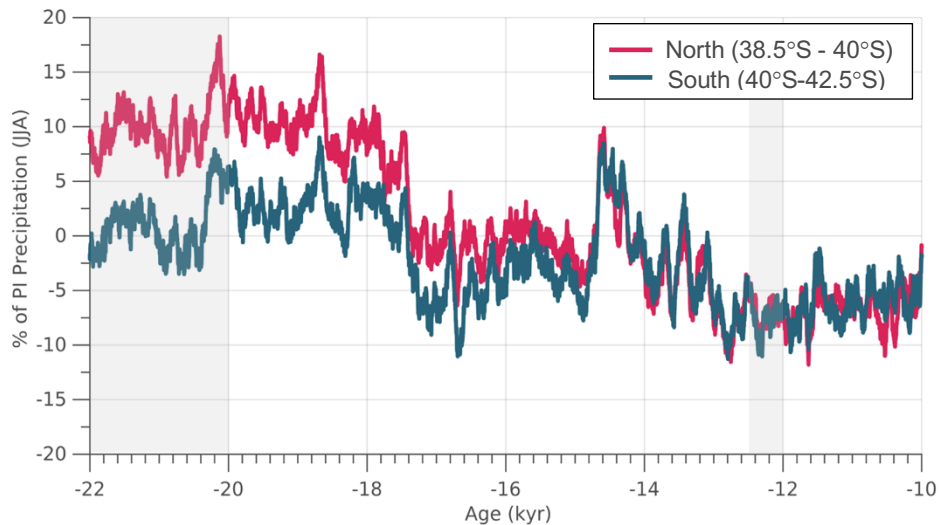


Figure 7. The winter (JJA) precipitation anomaly expressed as the percent difference from the preindustrial period. The area averaged anomaly is shown for the region north of 40°S and for the region south of 40°S (see Figure 2 for reference to the latitudinal range of our model domain). Intervals of time used in the sensitivity tests are highlighted by the gray shading.

412 *Precip. PI:* Monthly precipitation is held constant at the preindustrial mean. Preindustrial
413 precipitation is reduced compared to the period 22 ka to 18 ka, but is similar to and higher than
414 what is simulated after 18 ka for the exception of the ACR at 14.5 ka (Figure 7).

415 *Precip. 12 ka*: Monthly precipitation is held constant at the 12.5 ka-12 ka mean. This is a
416 period of reduced precipitation relative to the preindustrial (~7% reduction; Figure 7).

417 *Precip LGM*: Monthly precipitation is held constant to the 22-20 ka mean, which is
418 approximately 10% higher than preindustrial values across the Northern portion of the model
419 domain (North of 40°S).

420 Across our model domain during experiment *Precip. PI* (Figure 8A), wintertime precipitation
421 during the preindustrial is reduced compared to the early deglaciation (22 ka to 18ka) and is similar
422 to slightly higher particularly south of 40°S after 18 ka (Figure 7). When holding precipitation
423 constant at the preindustrial mean through the last deglaciation, the ice retreats faster across most
424 portions of the model domain, particularly along the ice margins and in area north of 40°S. In the
425 southern portion of our model domain (south of 40°S), where the changes in deglacial precipitation
426 relative to the preindustrial are lower (Figure 3 and 7), the difference in simulated deglaciation age
427 are also smaller. In general, the pace of deglaciation increases by up to 1 kyr compared to the
428 main simulation, with many locations experiencing deglaciation 200-600 yrs earlier than the main
429 simulation.

430

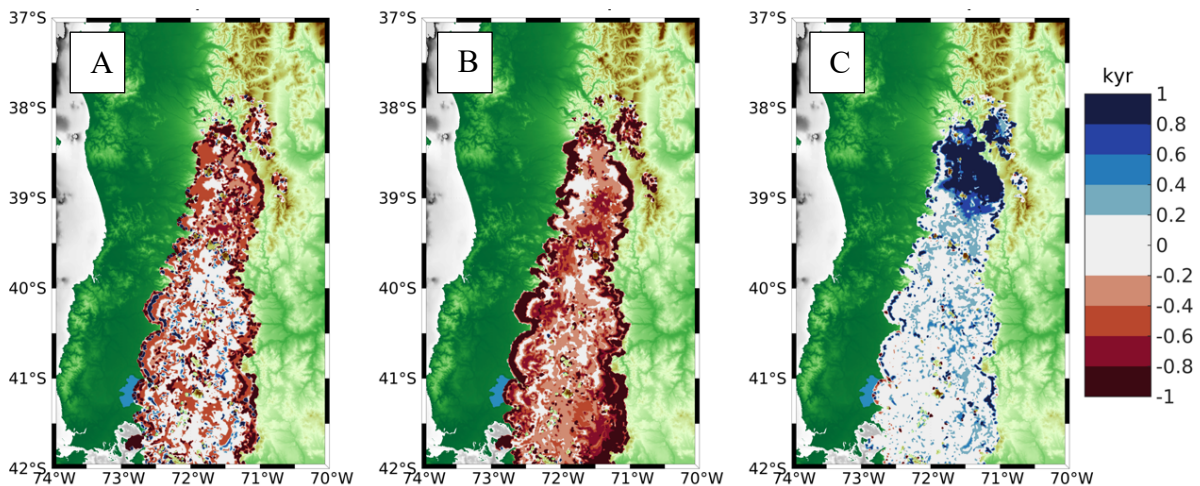


Figure 8. A) The difference in the simulated deglaciation age between sensitivity experiment *Precip. PI*; B.) experiment *Precip. 12 ka*, C.) and experiment *Precip LGM*, from the main simulation. Blue colors indicate slower ice retreat for the sensitivity experiments compared to the main simulation, while red colors indicate faster ice retreat for the sensitivity experiments compared to the main run.

431 For experiment *Precip. 12 ka*, winter precipitation is reduced by up to 7% (Figure 8B) relative to
432 the preindustrial across the model domain (Figure 3 and 7). In this experiment ice retreats faster
433 across most of the CLD, from the ice margins and through the interior. Deglaciation along the
434 margins occurs >1 kyr faster in many locations, and between 200 yrs to 1 kyr faster across portions
435 of the ice interior. For experiment *Precip LGM*, winter precipitation is increased by up to 10%
436 (Figure 8C; *Precip LGM*:) across the northern portion of the model domain (north of 40°S) relative
437 to preindustrial, but is similar to preindustrial values across the southern portion of our model
438 domain (south of 40°S). In this experiment, with the imposed higher precipitation across the

439 northern portion of the model domain, ice retreats slower during the last deglaciation relative to
440 our standard simulation by >1 kyr, and in some locations up to 2 kyr.

441 3.3 Comparison to the reconstructed deglacial ice extent

442
443 Shown in Figure 1, PATICE assigns high to medium confidence to the reconstructed LGM (25 ka
444 – 20 ka) ice extent along most of the western ice margin and portions of the eastern margin, with
445 low confidence assigned to the northernmost ice extent. The majority of the ice history is poorly
446 constrained (low confidence) during the deglaciation, and PATICE reconstructs a small cap that

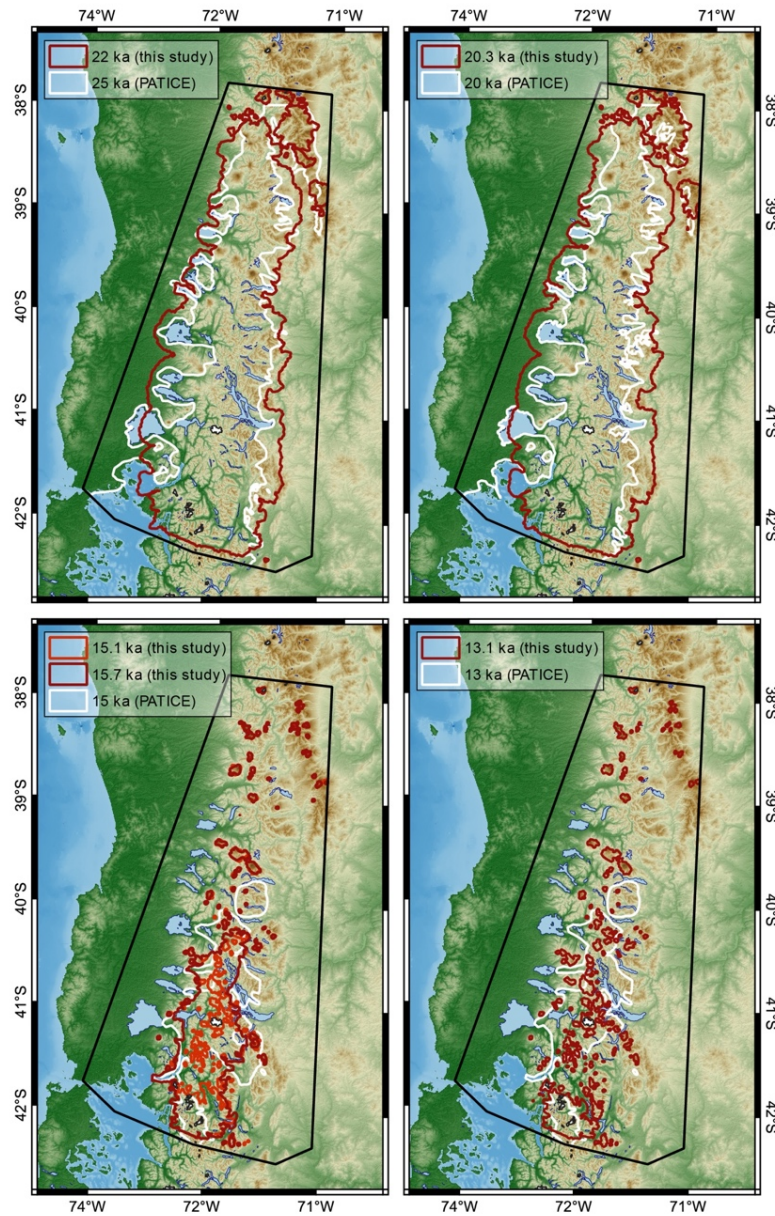


Figure 9. Comparison between the simulated ice extent at time intervals closest to the corresponding reconstructed ice extent from PATICE (Davies et al., 2020).

447 persists across the southern CLD until 10 ka, after which the ice disappears and only the Cerro
448 Tronador glacier remains (see Figure 13 from Davies et al., 2020). We show the simulated and
449 reconstructed ice extent in Figure 9 as well as the calculated ice area from PATICE at 20 ka, 15
450 ka, 13 ka, and 10ka and for our transient simulation in Figure 10. At 22 ka (Figure 9), our model
451 simulates a generally greater ice extent along the eastern and western margin, except at the Seno
452 de Reloncaví, Golfo de Ancud, and Lago Llanquihue, where the simulated ice margin does not
453 advance to the well dated terminal LGM moraines (Mercer, 1972; Porter, 1981; Andersen et al.,
454 1999; Denton et al., 1999). At 20 ka, the simulated ice area is $4.1 \times 10^4 \text{ km}^2$ which is nearly identical
455 to the PATICE areal extent across our model domain (Figure 10). The ice margin at the Seno de
456 Reloncaví, Lago Llanquihue, and other locations along the eastern boundary in the CLD advances
457 slightly at 20 ka, but still remain inboard of the PATICE reconstruction for these regions.

458
459 Between 18.3 ka and 15 ka large scale ice retreat occurs, and the simulated ice sheet loses 90% of
460 its ice area, while the PATICE reconstruction suggests a reduction of 75% (Figure 10). At 15 ka,
461 PATICE reconstructs an existing ice cap that separates from the remainder of the PIS to the south
462 (Figure 9). This is in contrast to the simulated ice extent, which shows that by 15 ka, the PIS
463 across our model domain has completely retreated and only mountain glaciers or small ice caps
464 exist amongst the high terrain. However, if we compare the PATICE area at 15 ka and the
465 simulated ice area at 15.7 ka (Figure 10; green rectangle), they are nearly identical at $1.2 \times 10^4 \text{ km}^2$.
466 While the PATICE ice extent at 15 ka and the simulated ice extent 15.7 ka do not match
467 completely, the simulated ice extent at 15.7 ka still has evidence of a large ice cap similar to the
468 PATICE reconstruction. Therefore, the simulated transition from ice sheet to ice cap and to
469 discrete mountain glaciers occurs between 15.7 ka and 15 ka in our simulations. By 13 ka, our
470 simulated ice area is 60% lower than the PATICE reconstructed area. By 10 ka this difference is
471 50%, however by this time the majority of the ice sheet has deglaciated (Figure 10), with our model
472 simulating discrete mountain glaciers while PATICE reconstructs a small and narrow ice cap
473 across the high terrain in the southern CLD (also see Figure 1).

474
475

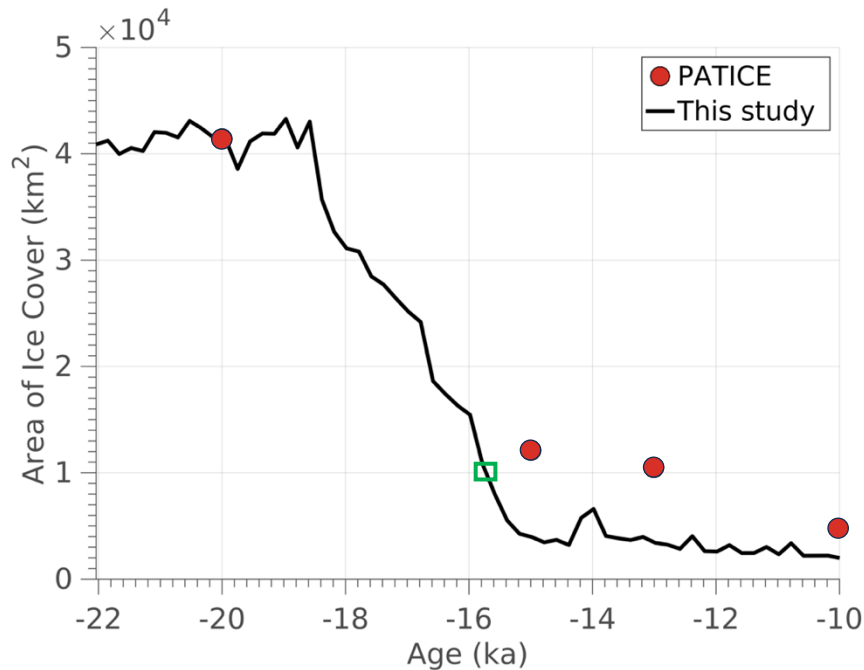


Figure 10. The simulated ice area (km²) from 22 ka to 10 ka shown as the black line. The red dots indicate the calculated ice area across our model domain for the reconstructed ice extent from PATICE (Davies et al., 2020). The green rectangle highlights the simulated ice area at 15.7 ka.

477

478 4 Discussion

479

480 4.1 Climate-ice sensitivity

481

482 Determining the influence of the SWW on the heat and hydrologic budget across South America
 483 during the LGM and last deglaciation remains difficult, as paleo-proxy data is limited and climate
 484 models tend to disagree on the evolution of the SWW (Kohfeld, 2013; Berman et al., 2018). And
 485 while paleo-proxy evidence does suggest wetter conditions across the CLD during the late glacial
 486 (Moreno and Videla, 2018), linking this variability to changes in the position and strength of the
 487 SWW remains difficult (Kohfeld et al., 2013).

488

489 The scale at which we deduce ice history and climate interactions is also important. Looking at
 490 the PIS as a whole, recent numerical ice sheet modelling studies indicate that the simulated ice
 491 extent and volume for the entire PIS at the LGM is largely controlled by the magnitude of the
 492 temperature anomaly compared to present day (Yan et al., 2022). However, regional scale ice
 493 flow modelling informed by geologic constraints on past ice margin extent show that higher
 494 precipitation during the LGM (Leger et al., 2021b), the late glacial, and the Holocene (Muir et al.,
 495 2023; Martin et al., 2022) is needed to support model-data agreement. It appears that during the
 496 LGM a northward shift in the SWW (Kohfeld et al., 2013; Rojas et al., 2009; Togweillier et al.,
 497 2006) or a strengthening or expansion of the wind belt (Lamy et al., 2010) is perhaps the most
 498 likely scenario, with high frequency variability possible during the deglaciation as atmospheric
 499 reorganization altered the heat and hydrologic budget as recorded by glacier and ice sheet change
 500 (Davies et al., 2020; Boex et al., 2013).

501 We analyzed outputs of the wintertime (JJA) 925 hPa zonal wind as the mean over 500 yr periods
502 from TraCE-21ka for the LGM (22-21ka), 18ka (18.5-18ka), 16ka (16.5-16ka), 14ka (14.5-14ka),
503 12ka (12.5-12ka) and the Preindustrial (Supplemental section 3, Figures S3 A-E). Across our
504 model domain and to its south, relative to the PI, zonal winds are stronger during the LGM with a
505 southerly displacement (Figure S3A first and second column). During 18ka (Figure S3B), the zonal
506 wind increases in strength relative to the PI, with the stronger winds having wider latitudinal
507 coverage, particularly across our model domain. While the mean position of the SWW is poleward
508 at 18ka relative to the PI (Jiang and Yan, 2022), across Patagonia the simulated position of the
509 maximum zonal wind is at the same latitudinal band as the PI. At 16ka, the zonal wind is stronger
510 across our domain and Patagonia (Figure S3C) relative to the PI, although not as large as the
511 differences during 18ka. By 14ka, the strength in the zonal winds across Patagonia and our model
512 domain are similar to slightly stronger than the PI (Figure S3D), however, the zonal wind
513 maximum is situated more equatorward across our model domain relative to the PI. By 12ka
514 (Figure S3E), the zonal wind is similar to slightly weaker than the PI across our model domain,
515 although it is stronger relative to the PI to the south of our model domain across central and
516 southern Patagonia. The position of the maximum zonal winds is also displaced further south
517 relative to the PI. These changes in strength and position of the simulated SWW during the last
518 deglaciation are similar to the findings of Jian and Yan (2020), which found that relative to the
519 Preindustrial (PI), TraCE-21ka simulates a more poleward subtropical and subpolar jet over the
520 Southern hemisphere at the LGM. During the remainder of the LGM and last deglaciation, the
521 overall position of the SWW migrates northward in TraCE-21ka, with poleward displacements
522 during Heinrich Stadial 1 (HS1), equatorward displacements during the Antarctic Cold Reversal
523 (ACR), and poleward displacements during the Younger Dryas (YD), similar to our analysis.

524
525 Additionally, we evaluated the wintertime (JJA) low-level (850 hPa) moisture flux convergence
526 from TraCE-21ka (MFC; Supplement section 4, Figure S4A-E), which is influenced by the mean
527 flow and transient eddies in the extratropical hydrologic cycle (Peixoto and Oort, 1992). During
528 the LGM and 18 ka, MFC increases across our model domain, consistent with a convergence of
529 the mean flow moisture fields relative to the PI (Figure S4 A, B). During the LGM and 18ka, we
530 note that TraCE-21ka simulates higher JJA precipitation anomalies (relative to the PI) across our
531 model domain (Figure 7). While our analysis cannot directly constrain the source of the positive
532 precipitation anomalies (e.g., mean flow, storms), the strength of the simulated SWW in TraCE-
533 21ka increases across our model domain (Figure S3 A, B) coincident with the increases in MFC,
534 which may contribute to the positive precipitation anomalies at these time intervals (Figure 7). By
535 16ka, there is increased divergence in the 925 hPa winds and moisture relative to the PI (Figure
536 S4 C). Decreased MFC relative to the PI coincides with a reduction in precipitation across our
537 model domain that is similar to or less than the PI (Figure 7). We note that the ice thickness
538 boundary conditions used in the TraCE-21ka come from the Ice5G reconstruction (Peltier, 2004),
539 which has the PIS being completely deglaciated by 16ka. However, our analysis cannot
540 decompose whether the simulated changes in precipitation and MFC are a consequence of the
541 coupling between regional atmospheric circulation and the ice thickness boundary conditions used
542 in TraCE-21ka or if these changes represent wider interactions with changes in hemispheric
543 atmospheric circulation. By 14ka, and during the ACR, MFC increases relative to the PI (Figure
544 S4D). This is consistent with a simulated equatorward migration of the SWW as shown in Jiang
545 and Yan (2020) and our analysis (Figure S3D), and positive anomalies in precipitation across our
546 model domain relative to the PI (Figure 7). By 12ka, precipitation across our model domain is

547 reduced relative to the PI (Figure 3 and 7), and TraCE-21ka simulates a reduction in the MFC as
548 well as a poleward migration of the SWW (Figure S3E; Jiang and Yan, 2020).

549
550 When considering proxy records of precipitation across the CLD, there is reasonable agreement
551 with the changes in precipitation simulated by TraCE-21ka. Moreno et al. (1999; 2015) and
552 Moreno and Videla (2018) find that wetter than present day conditions existed across the CLD
553 during the LGM and early deglaciation which is consistent with the precipitation anomalies
554 simulated by TraCE-21ka (Figure 3 and 7). These changes in paleoclimate proxies are attributed
555 to an intensified storm track associated with an equatorward shift of the SWW (Moreno et al. 1999;
556 2015). While TraCE-21ka instead simulates a poleward shift of the SWW during these time
557 intervals, increases in precipitation and the intensification of the storm track as inferred by Moreno
558 et al. (2015) may also be consistent with a strengthening of the SWW as simulated by TraCE-21ka
559 during these intervals (Figure S3 A, B; Rojas et al., 2009; Sime et al., 2013; Kohfeld et al., 2013).
560 Moreno et al. (2015) note that rapid warming ensues across the CLD around 17,800 cal yr BP,
561 which is similar to the timing of deglacial warming as simulated by TraCE-21ka around 18.5 ka
562 (Figure 6). Coincident with this rapid temperature rise, Moreno et al. (2015) note a shift from
563 hyper humid to humid conditions which aligns well with decreases in the simulated precipitation
564 in TraCE-21ka across our model domain (Figure 7). Lastly, Moreno et al. (1999; 2015) find that
565 colder and wetter conditions occur across the CLD during the ACR, and infer an equatorward
566 expansion of the SWW as a potential cause. While TraCE-21ka simulates an abrupt and short
567 ACR, it does simulate an equatorward expansion of the SWW (Figure S4 D; Jian and Yan, 2020),
568 associated cooling (Figure 6), and increases in precipitation (Figure 7) that agree with the proxy
569 data.

570
571 Prior numerical ice flow modelling has indicated that precipitation played an important role in
572 controlling the extent of paleoglaciers across the PIS (Muir et al., 2023; Leger et al., 2021b) by
573 modulating the pace and magnitude of ice retreat and advance during deglaciation (Martin et al.,
574 2022). Much of the TraCE-21ka simulated winter precipitation anomalies shown in Figure 3 and
575 7 are within 10% of the preindustrial value. The sensitivity tests conducted here suggest that
576 modest changes (~10%) in precipitation can alter the pace of ice retreat across the CLD on
577 timescales consistent with the resolution of geochronological proxies constraining past ice retreat.
578 We note that while TraCE-21ka simulates variations in precipitation across our model domain that
579 are consistent with hydroclimate proxies discussed above (Moreno et al., 1999; 2015; 2018), the
580 magnitude of those changes is not as large as proxy data across the CLD indicate. For example,
581 hydroclimate proxies suggest that the LGM and early deglaciation was up to 2 times wetter across
582 the CLD than present day (Moreno et al., 1999; Heusser et al., 1999). Therefore, we can deduce
583 from our sensitivity analysis here that higher precipitation anomalies during the LGM and last
584 deglaciation, forced by proposed changes in the SWW (Moreno et al., 1999; 2015), may have
585 helped offset melt from deglacial warming thereby influencing the pacing of early deglacial ice
586 retreat in this region.

587 588 ***4.2 Ice retreat during the Last Deglaciation***

589
590 The PATICE dataset (Davies et al., 2020) serves as the best available reconstruction of ice margin
591 change for the PIS across the last deglaciation. This state-of-the-art compilation provides an
592 empirical reconstruction of the configuration of the PIS as isochrones every 5 ka, from 35 ka to

593 present, based on detailed geomorphological data and available geochronological evidence.
594 Because geochronological constraints on past PIS change are limited, particularly in the CLD, the
595 PATICE reconstruction assigns qualitative confidence to its reconstructed ice margins. Where
596 there is agreement between geochronological and geomorphological indicators of past ice margin
597 history (i.e., moraines), high confidence is assigned. Where geomorphological evidence suggests
598 the existence of past ice margins, but lacks a geochronological constraint, medium confidence is
599 assigned. Lastly, low confidence is assigned where there is a lack of any indicators of past ice sheet
600 extent, where the ice limits result in interpolated interpretations from immediately adjacent
601 moraines from valleys that have been mapped and dated. Across the CLD, the LGM (25 ka, 20 ka)
602 ice extent is well constrained by geologic proxies particularly in the west and southwest (Figure
603 1). The moraines that constrain the piedmont ice lobes that formed along the western boundary
604 have reasonable age control (Denton et al., 1999; Moreno et al., 1999; Lowell et al., 1995), giving
605 confidence to the LGM ice margin limits. Beyond this region, age control is sparse along the
606 western boundary for the timing of LGM ice extent, but the existence of well-defined moraines
607 along lakes in the northern CLD are assumed to be in sync with those moraines deposited to the
608 south (Denton et al., 1999). However, low confidence remains in the geologic reconstruction of
609 the LGM ice boundary along the eastern margin where little to no chronological constraints are
610 available. In general, deglaciation from the maximum LGM ice extent begins between 18 – 19 ka
611 (Davies et al., 2020), however, poor age control and a lack of geomorphic indicators make it
612 difficult to constrain the ice extent across this region during the deglaciation. For instance, a single
613 cosmogenic nuclide surface exposure date retrieved from the Nahuel Huapi moraine yielded an
614 age of ~31.4 ka (Zech et al., 2017; 41.04° S, 71.15° W). While it is assumed that the ice limit
615 behaved similarly both to the west and east, the limited existing data prevents a comprehensive
616 understanding of the ice extent at the northeastern margin. This induces the highest level of
617 uncertainty in the reconstruction and hinders our data model comparison. Therefore, we rely on
618 the PATICE dataset interpolated isochrones (low confidence) for this northeastern region as the
619 state-of-the-art reconstruction.

620
621 In regards to ice area and extent, our simulated ice sheet at the LGM using TraCE-21ka climate
622 boundary conditions agrees well with the PATICE reconstruction (Figure 10). Our simulations
623 reveal that deglaciation began between 19 ka to 18 ka, consistent with the Davies et al. (2020)
624 reconstruction. Notably, the simulated timing of deglaciation agrees with moraine records further
625 south on the eastern side, such as in Río Corcovado (~43° S, Leger et al., 2021a), Río Cisnes (~44°
626 S, Garcia et al., 2019), Lago Palena/General Vintter (~44° S, Soteres et al., 2022), and Río
627 Ñirehuao (~45° S, Peltier et al., 2023). On the other hand, glaciers are thought to have withdrawn
628 from their LGM position later between ~18 - 17 ka on the northwestern margin (~41° S, Denton
629 et al., 1999; Moreno et al., 2015), in the southern (~46° S, Kaplan et al., 2004), and southernmost
630 regions (~52° S, McCulloch et al., 2000; 2005; Kaplan et al., 2008; Peltier et al., 2021). The
631 simulated ice retreat continues until 15 ka, with the largest pulses in ice mass loss occurring at 18.6
632 ka, 16.8 ka, and 16 ka (Figure 6). Where PATICE estimates an ice cap around 15 ka (~40°S), our
633 simulations reveal that glaciation was restricted to high elevations. After 15 ka, mountain glaciers
634 remain in our simulation but there is no presence of a large ice cap as reconstructed in PATICE.
635 Comparison between the model simulations and PATICE becomes difficult during the 15 -13 ka
636 period as confidence in the geologic reconstruction is low due to a lack of geochronological and
637 geomorphological constraints on past ice history. Therefore, our model results offer a different
638 reconstruction to PATICE, and indicate that the ice sheet in this region largely retreated by 15 ka,

639 with only mountain glaciers remaining. This is supported further south, where the ice sheet
640 disintegrated at ~16 ka with paleolake draining to the Pacific Ocean (~43° S, Leger et al., 2021a)
641 and the ice remaining limited to higher mountain areas. However, during this interval, the Antarctic
642 Cold Reversal (ACR) may have influenced the heat and hydrologic budget across this region, with
643 wetter and cooler conditions interrupting the deglacial warming (Moreno et al., 2018). While
644 TraCE-21ka simulates a cooler and wetter ACR, it is short-lived, lasting about 500 years as
645 compared to 2,000 years in some ice core records or proxy-based studies (Lowry et al., 2019; He
646 et al., 2013, Pedro et al., 2015). This potential for a favorable and prolonged period of glacier
647 growth is likely missing in our simulations during the ACR.
648

649 *4.3 Limitations*

650
651 Currently ISSM is undergoing model developments to include a full treatment of solid earth-ice
652 and sea-level feedbacks (Adhikari et al., 2016). Therefore, at this time, there is no coupling
653 between the ice sheet and solid earth. Instead, we prescribed GIA from a global GIA model of the
654 last glacial cycle from Caron et al. (2018). While this model reasonably estimates GIA across the
655 PIS over the last deglaciation, our simulated ice history does not feedback onto GIA. The ice
656 history for Patagonia incorporated into the Caron et al. (2018) ensemble is from Ivins et al. 2011.
657 Therefore, the prescribed GIA response across our domain does not perfectly match our simulated
658 ice history. Additionally, the global mantle from Caron et al. (2018) does not exhibit regional low
659 viscosity that is attributable to Patagonia and therefore, current rates of deformation are likely
660 underestimated by the model. By not simulating the 2-way coupled ice and solid-earth
661 interactions, we could be missing some feedbacks between our simulated ice history and the solid
662 earth that may modulate the deglaciation across this region. Despite this limitation however, our
663 prescribed GIA from Caron et al. (2018) is reasonable when compared with reconstructed deglacial
664 GIA in Patagonia (Troch et al., 2022; see Figure S2), giving confidence that our simulation is
665 capturing the regional influence of GIA on the simulated ice history.
666

667 Across most of our domain, moraines formed of glacio-tectonized outwash (Bentley, 1996)
668 provide evidence for an advance of piedmont glaciers across glacial outwash during the LGM,
669 which formed the physical boundary for some of the existing terminal moraines around the lakes
670 within the CLD (Bentley, 1996; Bentley, 1997). The formation of ice-contact proglacial lakes
671 likely occurred as a function of deglacial warming as ice retreated into overdeepenings in the
672 bedrock topography and filled with meltwater (Bentley, 1996). Where there were proglacial lakes
673 along the westward ice front in the CLD, evidence suggests that ice was grounded during the LGM
674 (Lago Puyehue; Heirman et al., 2011). During deglaciation, proglacial lakes formed along the ice
675 sheet margin (Bentley 1996,1997; Davies et al., 2020), with evidence suggesting that local
676 topography and calving may have influenced the spatially varying retreat rates along these margins
677 (Bentley, 1997). Recent glacier modelling (Sutherland et al., 2020) suggests that inclusion of ice-
678 lake interactions may have large impacts on the magnitude and rate of simulated ice front retreat,
679 as ice-lake interactions promote greater ice velocities, ice flux to the grounding line, and surface
680 lowering. However, it is not well constrained how the proglacial lakes in the CLD may have
681 influenced local deglaciation (Heirman et al., 2011). While more geomorphic data is needed,
682 recent work south of our study region (46.5°S) reconstructed early deglacial ice retreat using a
683 glaciolacustrine varve record from Lago General Carrera-Buenos Aires (Bendle et al., 2019). The
684 authors find that following initial retreat due to deglacial warming, the ice margin retreated into a

685 deepening proglacial lake which accelerated ice retreat in this region due to persistent calving,
686 therefore supporting the role proglacial lakes likely played across the margins of the retreating PIS
687 during the last deglaciation. Because the inclusion of ice-lake interactions is relatively novel for
688 numerical ice flow modeling (Sutherland et al., 2020; Quiquet et al., 2021; Hinck et al., 2022), we
689 choose to not simulate the evolution and influence of proglacial lakes on the deglaciation across
690 this model domain. Given this limitation, our simulated magnitude and rate of ice retreat at the
691 onset of deglaciation may be underestimated, especially when looking at local deglaciation along
692 these proglacial lakes. Although we do not think that these processes would greatly influence our
693 conclusions regarding the role of climate on the evolution of the PIS is the CLD and the simulated
694 ice retreat history, future work is required to assess the influence of proglacial lakes in this region.
695

696 **5 Conclusions**

697
698 In this study, we use a numerical ice sheet model to simulate the LGM and deglacial ice history
699 across the northernmost extent of the PIS, the CLD. The ice sheet model used inputs of
700 temperature and precipitation from the TraCE-21ka climate model simulation covering the last
701 22,000 years in order to simulate the deglaciation of the PIS across the CLD into the early
702 Holocene.
703

704 Our numerical simulation suggests that large scale ice retreat occurs after 19 ka coincident with
705 rapid deglacial warming, with the northern portion of the CLD becoming ice free by 17 ka. The
706 simulated ice retreat agrees well with the most comprehensive geologic assessment of past PIS
707 history available (PATICE; Davies et al., 2020) for the LGM ice extent and early deglacial but
708 diverge when considering the ice geometry at and after 15 ka. In our simulations, the PIS persists
709 until 15 ka across the remainder of the CLD, followed by ice retreat to higher elevations as
710 mountain glaciers and small ice caps persist into the early Holocene (e.g., Cerro Tronador). The
711 geologic reconstruction from PATICE instead estimates a small ice cap persisting across the
712 southern portion of high terrain in the CLD until about 10 ka. However, of the limited geologic
713 constraints particularly after 15 ka, high uncertainty in the timing and extent of deglacial ice history
714 remains in the geologic reconstruction. Therefore, our results provide an additional reconstruction
715 of the deglaciation of the PIS across the CLD that differs from PATICE after 15 ka, emphasizing
716 a need for future work that aims to improve geologic reconstructions of past ice margin migration
717 particularly during the later deglaciation across this region.
718

719 While deglacial warming was a primary driver of the demise of the PIS across the last deglaciation,
720 we find that precipitation modulates the pacing and magnitude of deglacial ice retreat across the
721 CLD. Paleoclimate proxies within the CLD has shown that the strength and position of the SWW
722 varied during the LGM and last deglaciation, altering hydrologic patterns and influencing the
723 deglacial mass balance. We find that the simulated changes in the strength and position of the
724 SWW in TraCE-21ka are similar to those inferred from paleoclimate proxies of precipitation,
725 consistent with a wetter than preindustrial climate being simulated and reconstructed over the CLD
726 and in particular the region north of 40°S. Through a series of sensitivity tests, we alter the
727 magnitude of the precipitation anomaly modestly (up to 10%) during our transient deglacial
728 simulations and find that the pacing of ice retreat can speed up or slow down by a few hundred
729 years and up to 2000 years depending on the imposed increase or decrease in the precipitation
730 anomaly. While paleoclimate proxies of precipitation suggest that the CLD may have experienced

731 twice as much precipitation during the LGM and early deglacial relative to present day (Moreno
732 et al.,1999;2015), TraCE-21ka simulates smaller increases in LGM and early deglacial
733 precipitation (~10-15% greater than preindustrial). Therefore, while our modelling suggests that
734 modest changes in precipitation can modulate the pace of deglacial ice retreat across the CLD,
735 from our analysis we can deduce that larger anomalies in precipitation as found in the paleoclimate
736 proxies may have an even larger impact on modulating deglacial ice retreat. Because paleoclimate
737 proxies of past precipitation are often lacking, and climate models can simulate a range of possible
738 LGM and deglacial hydrologic states, these results suggest that improved knowledge of the past
739 precipitation is critical towards better understanding the drivers of PIS growth and demise,
740 especially as small variations in precipitation can modulate ice sheet history on scales consistent
741 with geologic proxies.

742

743 **Code/Data Availability**

744 The simulations performed for this paper made use of the open-source Ice-Sheet and Sea-level
745 System Model (ISSM) and are publicly available at <https://issm.jpl.nasa.gov/> (Larour et al., 2012).

746

747 **Author Contribution**

748 JC and SM secured funding for this research. JC, MR, and SM all contributed to the project design.
749 JC performed the model setup and simulations. JC performed the analyses on model output, with
750 help from MR who performed analysis on PATICE reconstructions. JC wrote the manuscript with
751 input from MR and SM.

752

753 **Competing interests**

754 The contact author has declared that none of the authors has any competing interests.

755

756 **Acknowledgements**

757 This work was supported by a grant from the National Science Foundation, Frontier Research in
758 Earth Sciences # 2121561. We would like to thank Lambert Caron from the Jet Propulsion
759 Laboratory for his input regarding Glacial Isostatic Adjustment across our study region.

760

761 **References**

- 762 Adhikari, S., Ivins, E. R., and Larour, E., 2016, ISSM-SESAW v1.0: mesh-based computation of
763 gravitationally consistent sea level and geodetic signatures caused by cryosphere and
764 climate driven mass change, *Geoscientific Model Development*, 9, 9769-9816, doi:
765 10.5194/gmd-9-1087-2016.
- 766 Åkesson, H., Morlighem, M., Nisancioglu, K. H., Svendsen, J. J., and Mangerud, J.:
767 Atmosphere-driven ice sheet mass loss paced by topography: Insights from modelling the
768 south-western Scandinavian Ice Sheet. 2018. *Quaternary Sci. Rev.*, 195, 32–
769 47, <https://doi.org/10.1016/j.quascirev.2018.07.004>.
- 770 Andersen, B., Denton, G. H., & Lowell, T. V. (1999). Glacial geomorphologic maps of
771 Llanquihue drift in the area of the southern Lake District, Chile. *Geografiska Annaler:*
772 *Series A, Physical Geography*, 81(2), 155-166.
- 773 Bendle, J.M., Palmer, A.P., Thorndycraft, V.R., Matthews, I.P. 2019. Phased Patagonian Ice
774 Sheet response to Southern Hemisphere atmospheric and oceanic warming between 18
775 and 17 ka. *Sci. Rep.* 9, 4133. <https://doi.org/10.1038/s41598-019-39750-w>
- 776 Bentley, M.J., 1996. The role of lakes in moraine formation, Chilean Lake District. *Earth*

777 Surf. Process. Landf. 21, 493–507. [https://doi.org/10.1002/\(SICI\)1096-](https://doi.org/10.1002/(SICI)1096-)
778 9837(199606)21:6<493::AID-ESP612>3.0.CO;2-D

779 Bentley, M.J., 1997. Relative and radiocarbon chronology of two former glaciers in the
780 Chilean Lake District. *J. Quat. Sci.* 12, 25–33. [https://doi.org/10.1002/\(SICI\)1099-](https://doi.org/10.1002/(SICI)1099-)
781 1417(199701/02)12:1<25::AID-JQS289>3.0.CO;2-A

782 Berman, L., Silvestri, G., Tonello, M.S., On differences between Last Glacial Maximum and
783 Mid-Holocene climates in southern South America simulated by PMIP3 models. 2018.
784 *Quat. Sci. Rev.* 185, 113–121. <https://doi.org/10.1016/j.quascirev.2018.02.003>.

785 Blatter, H.: Velocity and stress-fields in grounded glaciers: A simple algorithm for including
786 deviatoric stress gradients. 1995. *J. Glaciol.*, 41, 333–344,
787 <https://doi.org/10.3189/S002214300001621X>

788 Boex, J., Fogwill, C., Harrison, S. et al. Rapid thinning of the late Pleistocene Patagonian Ice
789 Sheet followed migration of the Southern Westerlies. 2013. *Sci Rep* 3, 2118.
790 <https://doi.org/10.1038/srep02118>

791 Boisier, J. P., Alvarez-Garretón, C., Cepeda, J., Osses, A., Vásquez, N., and Rondanelli, R.:
792 CR2MET: A high-resolution precipitation and temperature dataset for hydroclimatic
793 research in Chile. 2018. EGUGA, p. 19739.

794 Braun, M.H., Malz, P., Sommer, C., Far.as-Barahona, D., Sauter, T., Casassa, G., Soruco,
795 A., Skvarca, P., Seehaus, T.C., 2019. Constraining glacier elevation and mass changes
796 in South America. *Nat. Clim. Chang.* 9, 130–136. <https://doi.org/10.1038/s41558-018->
797 0375-7

798 Brierley, C. M., Zhao, A., Harrison, S. P., Braconnot, P., Williams, C. J. R., Thornalley, D. J. R.,
799 Shi, X., Peterschmitt, J.-Y., Ohgaito, R., Kaufman, D. S., Kageyama, M., Hargreaves, J.
800 C., Erb, M. P., Emile-Geay, J., D'Agostino, R., Chandan, D., Carré, M., Bartlein, P. J.,
801 Zheng, W., Zhang, Z., Zhang, Q., Yang, H., Volodin, E. M., Tomas, R. A., Routson, C.,
802 Peltier, W. R., Otto-Bliesner, B., Morozova, P. A., McKay, N. P., Lohmann, G., Legrande,
803 A. N., Guo, C., Cao, J., Brady, E., Annan, J. D., and Abe-Ouchi, A.: Large-scale features
804 and evaluation of the PMIP4-CMIP6 *midHolocene* simulations, *Clim. Past*, 16, 1847–
805 1872, <https://doi.org/10.5194/cp-16-1847-2020>, 2020.

806 Briner, J. P., Cuzzone, J. K., Badgeley, J. A., Young, N. E., Steig, E. J., Morlighem, M.,
807 Schlegel, N.-J., Hakim, G., Schaefer, J. Johnson, J. V., Lesnek, A. L., Thomas, E. K.,
808 Allan, E., Bennike, O., Cluett, A. A., Csatho, B., de Vernal, A., Downs, J., Larour, E.,
809 and Nowicki, S.: Rate of mass loss from the Greenland Ice Sheet will exceed Holocene
810 values this century. 2020. *Nature*, 6, 70–74, <https://doi.org/10.1038/s41586-020-2742-6>.

811 Bondzio, J. H., Seroussi, H., Morlighem, M., Kleiner, T., Rückamp, M., Humbert, A., and
812 Larour, E. Y.: Modelling calving front dynamics using a level-set method: application to
813 Jakobshavn Isbræ, West Greenland. 2016. *The Cryosphere*, 10, 497–
814 510, <https://doi.org/10.5194/tc-10-497-2016>

815 Budd, W.F., P. L. Keage, N. A. Blundy. Empirical studies of ice sliding. 1979. *J. Glaciol.*,
816 23:157-170.

817 Caron, L., Ivins, E. R., Larour, E., Adhikari, S., Nilsson, J., and Blewitt, G.: GIA model statistics
818 for GRACE hydrology, cryosphere and ocean science. 2018. *Geophys. Res. Lett.*, 45,
819 2203–2212, <https://doi.org/10.1002/2017GL076644>

820 Choi, Y., Morlighem, M., Rignot, E., and Wood, M.: Ice dynamics will remain a primary driver
821 of Greenland ice sheet mass loss over the next century. 2021. *Commun. Earth Environ.*,
822 2, 26, <https://doi.org/10.1038/s43247-021-00092-z>

823 Clark, P.U., He, F., Golledge, N.R., Mitrovica, J.X., Dutton, A., Hoffman, J.S., and Dendy, S.,
824 2020, Oceanic forcing of penultimate deglacial and last interglacial sea-level rise: *Nature*,
825 v. 577, p. 660–664, doi:10.1038/s41586-020-1931-7.

826 Cuffey, K. M. and Paterson, W. S. B.: *The physics of glaciers*, 4th edn. 2010. Butterworth-
827 Heinemann, Oxford, ISBN 9780123694614

828 Cuzzone, J. K., Schlegel, N.-J., Morlighem, M., Larour, E., Briner, J. P., Seroussi, H., and Caron,
829 L.: The impact of model resolution on the simulated Holocene retreat of the southwestern
830 Greenland ice sheet using the Ice Sheet System Model (ISSM). 2019. *The Cryosphere*,
831 13, 879–893, <https://doi.org/10.5194/tc-13-879-2019>.

832 Cuzzone, J. K., Young, N. E., Morlighem, M., Briner, J. P., and Schlegel, N.-J.: Simulating the
833 Holocene deglaciation across a marine-terminating portion of southwestern Greenland in
834 response to marine and atmospheric forcings. 2022. *The Cryosphere*, 16, 2355–2372,
835 <https://doi.org/10.5194/tc-16-2355-2022>.

836 Davies, B.J., Darvill, C.M., Lovell, H., Bendle, J.M., Dowdeswell, J.A., Fabel, D.,
837 Gheorghiu, D.M., 2020. The evolution of the Patagonian ice sheet from 35 ka to
838 the present day (PATICE). *Earth Sci. Rev.* 204, 103152. [https://doi.org/10.1016/](https://doi.org/10.1016/j.earscirev.2020.103152)
839 [j.earscirev.2020.103152](https://doi.org/10.1016/j.earscirev.2020.103152).

840 Darvill, C.M., Stokes, C.R., Bentley, M.J., Evans, D.J.A., Lovell, H. 1996. Dynamics of former
841 ice lobes of the southernmost Patagonian Ice Sheet based on glacial landsystems
842 approach. *Journal of Quaternary Science.* 32, 6, 857-876.
843 <https://doi.org/10.1002/jqs.2890>

844 Darvill, C.M., Stokes, C.R., Bentley, M.J., Evans, D.J.A., Lovell, H., Dynamics of former ice
845 lobes of the southernmost Patagonian Ice Sheet based on glacial landsystems approach.
846 2017. *J. Quaternary Sci.*, 32:857-876. <https://doi.org/10.1002/jqs.2890>

847 Denton, G.H., Lowell, T.V., Heusser, C.J., Schlüchter, C., Andersen, B.G., Heusser, L.E.,
848 Moreno, P.I., Marchant, D.R., 1999. Geomorphology, Stratigraphy, and Radiocarbon
849 Chronology of Llanquihue Drift in the Area of the Southern Lake District, Seno
850 Reloncav., and Isla Grande de Chilo., Chile. *Geogr. Ann. Ser. A Phys. Geogr.* 81,
851 167–229. <https://doi.org/10.1111/1468-0459.00057>

852 Denton, G.H., Heusser, J., Lowell, T.V., Moreno, P.I., Andersen, B.G., Heusser, L.E., Schlüchter,
853 C., Marchant, D.R. 1999. Interhemispheric Linkage of Paleoclimate During the Last
854 Glaciation. *Geografiska Annaler.* 81, 2, 107-153. [https://doi.org/10.1111/1468-](https://doi.org/10.1111/1468-0459.00055)
855 [0459.00055](https://doi.org/10.1111/1468-0459.00055)

856 Dias dos Santos, T., Morlighem, M., and Brinkerhoff, D.: A new vertically integrated MONo-
857 Layer Higher-Order (MOLHO) ice flow model. 2022. *The Cryosphere*, 16, 179–195,
858 <https://doi.org/10.5194/tc-16-179-2022>.

859 Díaz, C., Moreno, P. I., Villacís, L. A., Sepúlveda-Zúñiga, E. A., & Maidana, N. I. (2023).
860 Freshwater diatom evidence for Southern Westerly Wind evolution since~ 18 ka in
861 northwestern Patagonia. *Quaternary Science Reviews*, 316, 108231.

862 Fernandez, A., Mark, B.G. 2016. Modeling modern glacier response to climate changes along the
863 Andes Cordillera: A multiscale review, *J. Adv. Model. Earth Syst.*, 8, 467–495,
864 doi:10.1002/2015MS000482.

865 García, J. L., Maldonado, A., De Porrás, M. E., Delaunay, A. N., Reyes, O., Ebersperger, C. A.,
866 Binnie, Lüthgens, C., S.A., Méndez, C. 2019. Early deglaciation and paleolake history of
867 Río Cisnes glacier, Patagonian ice sheet (44 S). *Quaternary Research*, 91(1), 194-217.
868 <https://doi.org/10.1017/qua.2018.93>.

869
870 Garreaud, R., Lopez, P., Minvielle, M., & Rojas, M. (2013). Large-scale control on the
871 Patagonian climate. *Journal of Climate*, 26(1), 215-230.
872 GEBCO Bathymetric Compilation Group 2021. 2021. The GEBCO_2021 Grid - a continuous
873 terrain model of the global oceans and land. NERC EDS British Oceanographic Data
874 Centre NOC. doi:10.5285/c6612cbe-50b3-0cff-e053-6c86abc09f8f
875 Glasser, N. F., Jansson, K. N., Harrison, S., & Kleman, J. (2008). The glacial geomorphology
876 and Pleistocene history of South America between 38 S and 56 S. *Quaternary Science*
877 *Reviews*, 27(3-4), 365-390.
878 Glen, J. W. The creep of polycrystalline ice. 1955. *P. Roy. Soc. Lond. A*, 228, 519–
879 538, <https://doi.org/10.1098/rspa.1955.0066>.
880 Golledge, N. R., Thomas, Z. A., Levy, R. H., Gasson, E. G. W., Naish, T. R., McKay, R. M.,
881 Kowalewski, D. E., and Fogwill, C. J.: Antarctic climate and ice-sheet configuration
882 during the early Pliocene interglacial at 4.23 Ma, *Clim. Past*, 13, 959–975,
883 <https://doi.org/10.5194/cp-13-959-2017>, 2017.
884 Hartmann, D. and Lo, F. Wave-Driven Zonal Flow Vacillation in the Southern Hemisphere.
885 1998. *Journal of the Atmospheric Sciences*. 55, 8, 1303-1315.
886 [https://doi.org/10.1175/1520-0469\(1998\)055<1303:WDZFVI>2.0.CO;2](https://doi.org/10.1175/1520-0469(1998)055<1303:WDZFVI>2.0.CO;2)
887 Hajima, T., Watanabe, M., Yamamoto, A., Tatebe, H., Noguchi, M. A., Abe, M., Ohgaito, R.,
888 Ito, A., Yamazaki, D., Okajima, H., Ito, A., Takata, K., Ogochi, K., Watanabe, S., and
889 Kawamiya, M.: Development of the MIROC-ES2L Earth system model and the
890 evaluation of biogeochemical processes and feedbacks, *Geosci. Model Dev.*, 13, 2197–
891 2244, <https://doi.org/10.5194/gmd-13-2197-2020>
892 He, F., Shakun, J. D., Clark, P. U., Carlson, A. E., Liu, Z., Otto-Bliesner, B. L., Kutzbach, J. E.
893 2013. Northern Hemisphere forcing of Southern Hemisphere climate during the last
894 deglaciation, *Nature*, 494, 81–85. doi: 10.1038/nature11822.
895 He, F., Clark, P.U. 2022. Freshwater forcing of the Atlantic Meridional Overturning Circulation
896 revisited. *Nature Climate Change*. 12. 449-454. [https://doi.org/10.1038/s41558-022-](https://doi.org/10.1038/s41558-022-01328-2)
897 [01328-2](https://doi.org/10.1038/s41558-022-01328-2).
898 Heirman, K., De Batist, M., Charlet, F., Moernaut, J., Chapron, E., Brümmer, R., Pino, M.,
899 Urrutia, R., 2011. Detailed seismic stratigraphy of Lago Puyehue: implications for the
900 mode and timing of glacier retreat in the Chilean Lake District. *J. Quat. Sci.* 26,
901 665–674. <https://doi.org/10.1002/jqs.1491>
902 Hinck, S., Gowan, E. J., Zhang, X., and Lohmann, G.: PISM-LakeCC: Implementing an adaptive
903 proglacial lake boundary in an ice sheet model. 2022. *The Cryosphere*, 16, 941–965,
904 <https://doi.org/10.5194/tc-16-941-2022>.
905 Hubbard, A., Hein, A.S., Kaplan, M.R., Hulton, N.R.J., Glasser, N., 2005. A modelling
906 reconstruction of the last glacial maximum ice sheet and its deglaciation in the
907 vicinity of the northern patagonian icefield, south America. *Geogr. Ann. Phys.Geogr.* 87
908 (2), 375-391. <https://doi.org/10.1111/j.0435-3676.2005.00264.x>
909 Hulton, N.R.J., Purves, R., McCulloch, R., Sugden, D.E., Bentley, M.J., 2002. The last
910 glacial maximum and deglaciation in southern south America. *Quat. Sci. Rev.* 21
911 (1), 233-241. [https://doi.org/10.1016/S0277-3791\(01\)00103-2](https://doi.org/10.1016/S0277-3791(01)00103-2).
912 Hulton, N., Sugden, D., Payne, A., Clapperton, C., 1994. Glacier modeling and the
913 climate of Patagonia during the last glacial maximum. *Quat. Res.* 42 (1), 1-19.
914 doi:10.1006/qres.1994.1049

- 915 Jiang, N., Yan, Q. Evolution of the meridional shift of the subtropical and subpolar westerly jet
 916 over the Southern Hemisphere during the past 21,000 years. 2020. *Quat Sci. Rev.* 246,
 917 <https://doi.org/10.1016/j.quascirev.2020.106544>.
- 918 Kaplan, M. R., Ackert Jr, R. P., Singer, B. S., Douglass, D. C., & Kurz, M. D. 2004. Cosmogenic
 919 nuclide chronology of millennial-scale glacial advances during O-isotope stage 2 in
 920 Patagonia. *Geological Society of America Bulletin*, 116(3-4), 308-321. doi:
 921 10.1130/B25178.1
- 922 Kaplan, M. R., Fogwill, C. J., Sugden, D. E., Hulton, N. R. J., Kubik, P. W., & Freeman, S. P. H.
 923 T. 2008. Southern Patagonian glacial chronology for the Last Glacial period and
 924 implications for Southern Ocean climate. *Quaternary Science Reviews*, 27(3-4), 284-294.
 925 <https://doi.org/10.1016/j.quascirev.2007.09.013>
- 926 Kilian, R., Lamy, F., 2012. A review of Glacial and Holocene paleoclimate records
 927 from southernmost Patagonia (49e55 S). *Quat. Sci. Rev.* 53,
 928 doi.10.1016/j.quascirev.2012.07.017
- 929 Kageyama, M., Harrison, S. P., Kapsch, M.-L., Lofverstrom, M., Lora, J. M., Mikolajewicz, U.,
 930 Sherriff-Tadano, S., Vadsaria, T., Abe-Ouchi, A., Bouttes, N., Chandan, D., Gregoire, L.
 931 J., Ivanovic, R. F., Izumi, K., LeGrande, A. N., Lhardy, F., Lohmann, G., Morozova, P.
 932 A., Ohgaito, R., Paul, A., Peltier, W. R., Poulsen, C. J., Quiquet, A., Roche, D. M., Shi,
 933 X., Tierney, J. E., Valdes, P. J., Volodin, E., and Zhu, J. 2021. The PMIP4 Last Glacial
 934 Maximum experiments: preliminary results and comparison with the PMIP3 simulations,
 935 *Clim. Past*, 17, 1065–1089, <https://doi.org/10.5194/cp-17-1065-2021>.
- 936 Kilian, R., Lamy, F. A review of Glacial and Holocene paleoclimate records from southernmost
 937 Patagonia (49-55°S). 2012. 53, 15, 1-23.
 938 <https://doi.org/10.1016/j.quascirev.2012.07.017>
- 939 Kohfeld, K.E., Graham, R.M., Boer, A. M. de, Sime, L.C., Wolff, E.W., Qu er e, C.L.,
 940 Bopp, L., 2013. Southern Hemisphere westerly wind changes during the Last
 941 Glacial Maximum: paleo-data synthesis. *Quat. Sci. Rev.* 68, 76-95. ,
 942 10.1016/j.quascirev.2013.01.017
- 943 Lamy, F., Kilian, R., Arz, H.W., Francois, J.-P., Kaiser, J., Prange, M., Steinke, T., 2010.
 944 Holocene changes in the position and intensity of the southern westerly wind belt. *Nat.*
 945 *Geosci.* 3, 695–699. <https://doi.org/10.1038/ngeo959>
- 946 Lamy, F., Arz, H. W., Kilian, R., Lange, C. B., Lembke-Jene, L., Wengler, M., ... & Tiedemann,
 947 R. (2015). Glacial reduction and millennial-scale variations in Drake Passage
 948 throughflow. *Proceedings of the National Academy of Sciences*, 112(44), 13496-13501
 949 <https://doi.org/10.1073/pnas.1509203112>
- 950 Larour, E., Seroussi, H., Morlighem, M., and Rignot, E.: Continental scale, high order, high
 951 spatial resolution, ice sheet modeling using the Ice Sheet System Model (ISSM). 2012. *J.*
 952 *Geophys. Res.-Earth*, 117, F01022, <https://doi.org/10.1029/2011JF002140>
- 953 Le Morzadec, K., Tarasov, L., Morlighem, M., and Seroussi, H.: A new sub-grid surface mass
 954 balance and flux model for continental-scale ice sheet modelling: testing and last glacial
 955 cycle. 2015. *Geosci. Model Dev.*, 8, 3199–3213, [https://doi.org/10.5194/gmd-8-3199-](https://doi.org/10.5194/gmd-8-3199-2015)
 956 2015
- 957 Leger, T. P., Hein, A. S., Bingham, R. G., Rodés, Á., Fabel, D., & Smedley, R. K. 2021a.
 958 Geomorphology and 10Be chronology of the Last Glacial Maximum and deglaciation in
 959 northeastern Patagonia, 43° S-71° W. *Quaternary Science Reviews*, 272, 107194.
 960 DOI:[10.1016/j.quascirev.2021.107194](https://doi.org/10.1016/j.quascirev.2021.107194)

- 961 Leger TPM, Hein AS, Goldberg D, Schimmelpfennig I, Van Wyk de Vries MS, Bingham RG and
 962 ASTER Team. 2021b. Northeastern Patagonian Glacier Advances (43°S) Reflect
 963 Northward Migration of the Southern Westerlies Towards the End of the Last Glaciation.
 964 *Front. Earth Sci.* 9:751987. doi: 10.3389/feart.2021.751987
- 965 Liu, Z., Otto-Bliesner, B., He, F., Brady, E., Tomas, R., Clark, P., Carlson, A., Lynch-Stieglitz,
 966 J., Curry, W., Brook, E., Erickson, D., Jacob, R., Kutzbach, J., and Cheng, J. 2009.
 967 Transient simulation of last deglaciation with a new mechanism for Bølling-Allerød
 968 warming, *Science*, 325, 310–314. <https://doi.org/10.1126/science.1171041>
- 969 Lowry, D. P., Golledge, N. R., Menviel, L., and Bertler, N. A. N.: Deglacial evolution of
 970 regional Antarctic climate and Southern Ocean conditions in transient climate
 971 simulations. 2019. *Clim. Past*, 15, 189–215, <https://doi.org/10.5194/cp-15-189-2019>.
- 972 Lowell, T., Heusser, C., Andersen, B., Moreno, P., Hauser, A., Heusser, L., Schlüchter,
 973 C., Marchant, D., Denton, G., 1995. Interhemispheric correlation of late Pleistocene glacial
 974 events. *Science* 269, 1541–1549. Doi: 10.1126/science.269.5230.1541
- 975 Lowry, D. P., Golledge, N. R., Menviel, L., and Bertler, N. A. N.: Deglacial evolution of
 976 regional Antarctic climate and Southern Ocean conditions in transient climate
 977 simulations. 2019. *Clim. Past*, 15, 189–215, <https://doi.org/10.5194/cp-15-189-2019>
- 978 Marcott, S.A., Shakun, J.D., Clark, P.U., Mix, A.C. 2013. A Reconstruction of Regional and
 979 Global Temperature for the Past 11,300 Years. 339, 6124, 1198-1201. DOI:
 980 10.1126/science.1228026
- 981 Martin J, Davies BJ, Jones R and Thorndycraft V (2022), Modelled sensitivity of Monte San
 982 Lorenzo ice cap, Patagonian Andes, to past and present climate. *Front. Earth Sci.*
 983 10:831631. doi: 10.3389/feart.2022.831631
- 984 Mauritsen, T., Bader, J., Becker, T., Behrens, J., Bittner, M., Brokopf, R., Brovkin, V., Claussen,
 985 M., Crueger, T., Esch, M., Fast, I., Fiedler, S., Fläschner, D., Gayler, V., Giorgetta, M.,
 986 Goll, D. S., Haak, H., Hagemann, S., Hedemann, C., Hohenegger, C., Ilyina, T., Jahns, T.,
 987 Jimenez-de-la-Cuesta, D., Jungclaus, J., Kleinen, T., Kloster, S., Kracher, D., Kinne, S.,
 988 Kleberg, D., Lasslop, G., Kornbluh, L., Marotzke, J., Matei, D., Meraner, K.,
 989 Mikolajewicz, U., Modali, K., Möbis, B., Müller, W. A., Nabel, J. E. M. S., Nam, C. C.
 990 W., Notz, D., Nyawira, S.-S., Paulsen, H. Peters, K., Pincus, R., Pohlmann, H. Pongratz,
 991 J., Popp, M., Raddatz, T. J., Rast, S., Redler, R., Reick, C. H., Rohrschneider, T.,
 992 Schemann, V., Schmidt, H., Schnur, R., Schulzweida, U., Six, K. D., Stein, L., Stemmler,
 993 I., Stevens, B., von Storch, J.-S., Tian, F., Voigt, A., Vrese, P., Wieners, K.-H.,
 994 Wilkenskjaeld, S., Winkler, A., and Roeckner, E.: Developments in the MPI-M Earth
 995 System Model version 1.2 (MPI-ESM1.2) and its response to increasing CO₂, *J. Adv.*
 996 *Model. Earth Syst.* 2019. 11, 998–1038, <https://doi.org/10.1029/2018MS001400>
- 997 McCulloch, R. D., Bentley, M. J., Purves, R. S., Hulton, N. R., Sugden, D. E., & Clapperton, C.
 998 M. (2000). Climatic inferences from glacial and palaeoecological evidence at the last
 999 glacial termination, southern South America. *Journal of Quaternary Science: Published*
 1000 *for the Quaternary Research Association*, 15(4), 409-417.
 1001 <https://doi.org/10.1002/jqs.608>
- 1002 McCulloch, R. D., Fogwill, C. J., Sugden, D. E., Bentley, M. J., & Kubik, P. W. (2005).
 1003 Chronology of the last glaciation in central Strait of Magellan and Bahía Inútil,
 1004 southernmost South America. *Geografiska Annaler: Series A, Physical*
 1005 *Geography*, 87(2), 289-312. <https://doi.org/10.1111/j.0435-3676.2005.00260.x>

1006 Meier, W.J-H., Griesinger, J., Hochreuther, P., Braun, M.H. 2018. An updated multi-temporal
1007 glacier inventory for the Patagonian Andes with changes between the Little Ice Age and
1008 2016. *Frontiers in Earth Science*, 6, 62. <https://doi.org/10.3389/feart.2018.00062>

1009 Menviel, L., A. Timmermann, A. Mouchet, and O. Timm, 2008: Climate and marine carbon
1010 cycle response to changes in the strength of the Southern Hemispheric
1011 westerlies. *Paleoceanography*, **23**, PA4201, doi:10.1029/2008PA001604.

1012 Mercer, J.H., 1972. Chilean glacial chronology 20,000 to 11,000 carbon-14 years ago:some
1013 global comparisons. *Science* 176, 1118–1120. DOI: 10.1126/science.176.4039.1118

1014 Moreno, P. I., Lowell, T. V., Jacobson Jr, G. L., & Denton, G. H. (1999). Abrupt vegetation and
1015 climate changes during the last glacial maximum and last termination in the Chilean lake
1016 district: a case study from Canal de la Puntilla (41°S). *Geografiska Annaler: Series A,*
1017 *Physical Geography*, 81(2), 285-311.

1018 Moreno, P.I., Denton, G.H., Moreno, H., Lowell, T.V., Putnam, A.E., Kaplan, M.R., 2015.
1019 Radiocarbon chronology of the last glacial maximum and its termination in
1020 northwestern Patagonia. *Quat. Sci. Rev.* 122, 233e249. 10.1016/j.quascirev.2015.05.027

1021 Moreno, P.I., Videla, J., Valero-Garcés, B.L., Alloway, B.V., Heusser, L.E., 2018.
1022 A continuous record of vegetation, fire-regime and climatic changes in northwestern
1023 Patagonia spanning the last 25,000 years. *Quat. Sci. Rev.* 198,
1024 10.1016/j.quascirev.2018.08.013

1025 Morlighem, M., Bondzio, J., Seroussi, H., Rignot, E., Larour, E., Humbert, A., and Rebuffi, S.:
1026 Modeling of Store Gletscher's calving dynamics, West Greenland, in response to ocean
1027 thermal forcing. 2016. *Geophys. Res. Lett.*, 43, 2659–
1028 2666, <https://doi.org/10.1002/2016GL067695>

1029 Muir, R., Eaves, S., Vargo, L., Anderson, B., Mackintosh, A., Sagredo, E., Soteres, R. Late
1030 glacial climate evolution in the Patagonian Andes (44-47°S) from alpine glacier modelling.
1031 2023. *Quaternary Science Reviews*, 305, <https://doi.org/10.1016/j.quascirev.2023.108035>.

1032 Ohgaito, R., Yamamoto, A., Hajima, T., Oishi, R., Abe, M., Tatebe, H., Abe-Ouchi, A., and
1033 Kawamiya, M.: PMIP4 experiments using MIROC-ES2L Earth system model, *Geosci.*
1034 *Model Dev.*, 14, 1195–1217, <https://doi.org/10.5194/gmd-14-1195-2021>

1035 Pattyn, F.: A new three-dimensional higher-order thermomechanical ice sheet model:
1036 Basic sensitivity, ice stream development, and ice flow across subglacial lakes. 2003. *J.*
1037 *Geophys. Res.*, 108, 2382, <https://doi.org/10.1029/2002JB002329>

1038 Pedro, J. B., Bostock, H. C., Bitz, C. M., He, F., Vandergoes, M. J., Steig, E. J., Chase, B.M.,
1039 Krause, C.E., Rasmussen, S.O., Bradley, M.R., Cortese, G. 2016. The spatial extent and
1040 dynamics of the Antarctic Cold Reversal. *Nature Geoscience*, 9(1), 51-55.
1041 <https://doi.org/10.1038/ngeo2580>

1042 Peixoto, J. P., and A. H. Oort (1992), *Physics of Climate*, American Institute of Physics,
1043 520 pp.

1044 Peltier, C., Kaplan, M. R., Birkel, S. D., Soteres, R. L., Sagredo, E. A., Aravena, J. C., ... &
1045 Schaefer, J. M. (2021). The large MIS 4 and long MIS 2 glacier maxima on the southern
1046 tip of South America. *Quaternary Science Reviews*, 262, 106858.
1047 <https://doi.org/10.1016/j.quascirev.2021.106858> 0277-3791

1048 Peltier, C., Kaplan, M. R., Sagredo, E. A., Moreno, P. I., Araos, J., Birkel, S. D., ... & Schaefer,
1049 J. M. (2023). The last two glacial cycles in central Patagonia: A precise record from the
1050 Ñirehuao glacier lobe. *Quaternary Science Reviews*, 304, 107873.
1051 DOI:10.1016/j.quascirev.2022.107873

1052
1053 Pfeffer, W.T., Arendt, A.A., Bliss, A., Bolch, T., Cogley, J.G., Gardner, A.S., Hagen, J.O., Hock,
1054 R., Kaser, G., Kienholz, C. and Miles, E.S. 2014. The Randolph Glacier Inventory: a
1055 globally complete inventory of glaciers. *Journal of Glaciology*, 60, 537-552.
1056 Doi:10.313189/2014JoG13J176
1057 Pollard, D. and DeConto, R. M.: Description of a hybrid ice sheet-shelf model, and application to
1058 Antarctica. 2012. *Geosci. Model Dev.*, 5, 1273–1295, [https://doi.org/10.5194/gmd-5-](https://doi.org/10.5194/gmd-5-1273-2012)
1059 [1273-2012](https://doi.org/10.5194/gmd-5-1273-2012).
1060 Porter, S. C. (1981). Pleistocene glaciation in the southern Lake District of Chile. *Quaternary*
1061 *Research*, 16(3), 263-292.
1062 Quiquet, A., Dumas, C., Paillard, D., Ramstein, G., Ritz, C., and Roche, D. M.: Deglacial Ice
1063 Sheet Instabilities Induced by Proglacial Lakes. 2021. *Geophys. Res. Lett.*, 48,
1064 e2020GL092141, <https://doi.org/10.1029/2020GL092141>
1065 Rojas, M., Moreno, P., Kageyama, M., Crucifix, M., Hewitt, C., Abe-Ouchi, A., Ohgaito, R.,
1066 Brady, E.C., Hop, P. 2009. The Southern Westerlies during the last glacial maximum in
1067 PMIP2 simulations. *Clim. Dyn.* 32, 525–548. [https://doi.org/10.1007/s00382-008-0421-](https://doi.org/10.1007/s00382-008-0421-7)
1068 [7](https://doi.org/10.1007/s00382-008-0421-7).
1069 Rojas, M., 2013. Sensitivity of southern Hemisphere circulation to LGM and 4 CO₂
1070 climates. *Geophys. Res. Lett.* 40, 965e970.
1071 Sepulchre, P., Caubel, A., Ladant, J.-B., Bopp, L., Boucher, O., Braconnot, P., Brockmann, P.,
1072 Cozic, A., Donnadieu, Y., Dufresne, J.-L., Estella-Perez, V., Ethé, C., Fluteau, F.,
1073 Foujols, M.-A., Gastineau, G., Ghattas, J., Hauglustaine, D., Hourdin, F., Kageyama, M.,
1074 Khodri, M., Marti, O., Meurdesoif, Y., Mignot, J., Sarr, A.-C., Servonnat, J.,
1075 Swingedouw, D., Szopa, S., and Tardif, D.: IPSL-CM5A2 – an Earth system model
1076 designed for multi-millennial climate simulations, *Geosci. Model Dev.*, 2020. 13, 3011–
1077 3053, <https://doi.org/10.5194/gmd-13-3011-2020>
1078 Seguinot, J., Rogozhina, I., Stroeven, A. P., Margold, M., and Kleman, J.: Numerical simulations
1079 of the Cordilleran ice sheet through the last glacial cycle, *The Cryosphere*, 10, 639–664,
1080 <https://doi.org/10.5194/tc-10-639-2016>, 2016.
1081 Shakun, J., Clark, P., He, Marcott, S.A., Mix, A. C., Liu, A., Otto-Bliesner, B., Schmittner, A.,
1082 Bards, E. 2012. Global warming preceded by increasing carbon dioxide concentrations
1083 during the last deglaciation. *Nature* 484, 49–54. <https://doi.org/10.1038/nature10915>
1084 Shakun, J.D., Lea, D.W., Lisiecki, L.E., Raymo, M.E. 2015. An 800-kyr record of global
1085 surface ocean $\delta^{18}\text{O}$ and implications for ice volume-temperature coupling. 426, 58-68.
1086 <https://doi.org/10.1016/j.epsl.2015.05.042>
1087 Sidorenko, D., Goessling, H., Koldunov, N., Scholz, P., Danilov, S., Barbi, D., Cabos, W.,
1088 Gurses, O., Harig, S., Hinrichs, C., Juricke, S., Lohmann, G., Losch, M., Mu, L.,
1089 Rackow, T., Rakowsky, N., Sein, D., Semmler, T., Shi, X., Stepanek, C., Streffing, J.,
1090 Wang, Q., Wekerle, C., Yang, H., and Jung, T.: Evaluation of FESOM2.0 Coupled to
1091 ECHAM6.3: Preindustrial and High- ResMIP Simulations, 2019. *J. Adv. Model. Earth*
1092 *Sy.*, 11, 3794–3815, <https://doi.org/10.1029/2019MS001696>
1093 Sime, L. C., K. E. Kohfeld, C. Le Quéré, E. W. Wolff, A. M. de Boer, R. M. Graham,
1094 and L. Bopp, 2013: Southern Hemisphere westerly wind changes during the Last Glacial
1095 Maximum: Model–data comparison. *Quat. Sci. Rev.*, 64, 104–
1096 120, <https://doi.org/10.1016/j.quascirev.2012.12.008>.

1097 Sugden, D. E., N. R. J. Hulton, and R. S. Purves (2002), Modelling the inception of the
1098 Patagonian icesheet, *Quat. Int.*, 95 – 96, 55 – 64. DOI:10.1016/S0277-3791(01)00103-2
1099 Sutherland, J. L., Carrivick, J. L., Gandy, N., Shulmeister, J., Quincey, D. J., and Cornford, S. L.:
1100 Proglacial Lakes Control Glacier Geometry and Behavior During Recession. 2020.
1101 *Geophys. Res. Lett.*, 47, e2020GL088865, <https://doi.org/10.1029/2020GL088865>
1102 Tarasov, L. and Peltier, R. W.: Impact of thermomechanical ice sheet coupling on a model of the
1103 100 kyr ice age cycle. 1999. *J. Geophys. Res.-Atmos.*, 104, 9517–9545
1104 Tozer, B., Sandwell, D.T., Smith, W.H.F., Olsen, S.C., Beale, J.R., Wessel, P. Global
1105 Bathymetry and Topography at 15 Arc Sec: SRTM15+. 2019. *Earth and Space Science*.
1106 6, 10, 1847-1864. <https://doi.org/10.1029/2019EA000658>
1107 Tigchelaar, M., Timmermann, A., Friedrich, T., Heinemann, M., and Pollard, D.: Nonlinear
1108 response of the Antarctic Ice Sheet to late Quaternary Sea level and climate forcing, *The*
1109 *Cryosphere*, 13, 2615–2631, <https://doi.org/10.5194/tc-13-2615-2019>, 2019.
1110 Toggweiler, J.R., Russell, J.L., Carson, S.R. Midlatitude westerlies, atmospheric CO₂, and
1111 climate change during the ice ages. 2006. *Paleoceanography and Paleoclimatology*. 21,
1112 <https://doi.org/10.1029/2005PA001154>
1113 Troch, M., Bertrand, S., Lange, C.B., Cardenas, P., Arz, H., Pantoja-Gutierrez, S., De Pol-Holz
1114 R., Kilian, R. Glacial isostatic adjustment near the center of the former Patagonian Ice
1115 Sheet (48S) during the last 16.5 kyr. *Quaternary Science Reviews*. 277.
1116 <https://doi.org/10.1016/j.quascirev.2021.107346>
1117 Yan, Q., Wei, T., Zhang, Z. Modeling the climate sensitivity of Patagonian glaciers and their
1118 responses to climatic change during the global last glacial maximum. 2022. *Quat. Sci.*
1119 *Rev.*, 288. <https://doi.org/10.1016/j.quascirev.2022.107582>
1120 Zech, J., Terrizzano, C.M., García Morabito, E., Veit, H., Zech, R., 2017. Timing and extent of
1121 late Pleistocene glaciation in the arid Central Andes of Argentina and Chile (22°-41°S).
1122 *Geogr. Res. Lett.* 43, 697–718. <https://doi.org/10.18172/cig.3235>.
1123
1124
1125